IEEE Access
Multidisciplinary | Rapid Review | Open Access Journal

Received November 24, 2020, accepted December 12, 2020, date of publication December 16, 2020,
date of current version December 28, 2020.

Digital Object Identifier 10.1109/ACCESS.2020.3045327

Limits of Effective Material Properties in the Context of an Electromagnetic Tissue Model

KEVIN JERBIC, KEVIN NEUMANN, JAN TARO SVEJDA, BENEDIKT SIEVERT, (Member, IEEE), ANDREAS RENNINGS, AND DANIEL ERNI, (Member, IEEE)

General and Theoretical Electrical Engineering (ATE), Faculty of Engineering, University of Duisburg-Essen, 47048 Duisburg, Germany
Center for Nanointegration Duisburg-Essen (CENIDE), University of Duisburg-Essen, 47048 Duisburg, Germany

Corresponding author: Kevin Jerbic (kevin.jerbic@uni-due.de)

This work was supported in part by the Deutsche Forschungsgemeinschaft (DFG), German Research Foundation under Project 287022738 and Project TRR 196 MARIE in the framework of project (Project M03), and in part by the Open Access Publication Fund of the University of Duisburg-Essen.

ABSTRACT Most calibration schemes for reflection-based tissue spectroscopy in the mm-wave/THz-frequency range are based on homogenized, frequency-dependent tissue models where macroscopic material parameters have either been determined by measurement or calculated using effective material theory. However, as the resolution of measurement at these frequencies captures the underlying microstructure of the tissue, we will investigate the validity limits of such effective material models over a wide frequency range (10 MHz - 200 GHz). Embedded in a parameterizable virtual workbench, we implemented a numerical homogenization method using a hierarchical multiscale approach to capture both the dispersive and tensorial electromagnetic properties of the tissue, and determined at which frequency this homogenized model deviated from a full-wave electromagnetic reference model within the framework of a Monte-Carlo analysis. Simulations were carried out using a generic hypodermal tissue that emulated the morphology of the microstructure. Results showed that the validity limit occurred at surprisingly low frequencies and thus contradicted the traditional usage of homogenized tissue models. The reasons for this are explained in detail and thus it is shown how both the lower ''allowed'' and upper ''forbidden'' frequency ranges can be used for frequency-selective classification/identification of specific material and structural properties employing a supervised machine-learning approach. Using the implemented classifier, we developed a method to identify specific frequency bands in the forbidden frequency range to optimize the reliability of material classification.

INDEX TERMS Material classification, multiscale modelling, homogenization, mm-wave applications, machine learning.

I. INTRODUCTION

Contactless, non-invasive material characterization/classification based on reflectometry at mm-wave up to THz frequencies is currently gaining a great deal of interest due its potential to resolve both material and structural properties together with the increasing availability of mobile integrated electronic systems in these particular frequency ranges [1]. Recent progress in mm-wave/THz reflectometry has led, e.g., to high-precision bulk material characterization of various dielectrics in the mm-wave range of 200 GHz - 250 GHz using, e.g., a model-based calibration scheme [2], [3]. Broadband THz time-domain spectroscopy (THz-TDS) systems operating in reflection mode in the range of 60 GHz up to 4 THz have been successfully employed to, e.g., analyze delamination in glass fiber-reinforced composite [4], [5], or in food inspection to reliably distinguish transgenic from non-transgenic rice seeds using machine learning-based classification of spectral fingerprints [6], [7]. An important field of application, which has been thoroughly investigated in recent years, is the extensive use of mm-wave/THz reflectometry for non-invasive tissue diagnostics [8], [9]. Most of the described approaches retrieve dielectric spectroscopy data using calibration schemes based

The associate editor coordinating the review of this manuscript and approving it for publication was Taous Meriem Laleg-kirati.

on homogenized, frequency-dependent tissue models. Such model-based refinement becomes increasingly important when the proper structure of complex tissue morphologies is under consideration [10]. A comprehensive review of the current progress of e.g. mm-wave/THz-based diagnosis of tumorous tissue and neoplasms (beyond the abnormal tissue's water signature) is given in [11]. The biological tissue can thus be viewed as a bona fide benchmark problem for reflectometry-based material characterization especially at mm-wave/THz frequencies with respect to the structural complexity at different length scales, the large variety of its constituents with associated losses and material contrasts, and the inherent anisotropy at the cell level up to the layer structure.

In the mm-wave/THz reflectometry scenarios mentioned, the role of holistic multiscale tissue models based on computational electromagnetics (EM) is therefore becoming increasingly important to maximize the sensitivity and selectivity achieved by machine learning and regression analysis approaches. The major challenge in developing such a tissue model concerns the complex multiscale morphology of the skin, which determines its macroscopic EM properties. Most of the current EM skin models follow a heuristic representation of the skin topology as a multi-layer structure as proposed by Alekseev *et al.* [12] containing typically 3 to 4 homogenized dispersive layers. The material parameters of the latter are retrieved either from fitting models to experimental data [12] or in the framework of the effective material theory (EMT) using extended analytic mixing rules with associated multipole Debye models (e.g. the Havriliak-Negami relationship [13]) to account for the corresponding frequency dependence. A more rigorous approach builds upon a hierarchically organized multiscale EM model that is rooted in the skin's proper cellular structure. This is used in conjunction with a numerical homogenization procedure of the tissue's microstructure with the aim of determining both the dispersive and tensorial EM material properties. Such a multiscale approach has been pioneered by Huclova *et al.* [14] for human tissue analysis up to 1 GHz including the full skin layer morphology together with macroscopic textures like, e.g., the upper and deeper vessel plexus [15] to determine sensitivity and specificity of changes in skin components [16]. An extension to this model up to 1 THz has been provided by Saviz *et al.* [17] using classical mixing rules for the homogenization of the various tissue layers, and was later complemented by Spathmann *et al.* [18] to include macroscopic features such as hair follicles and skin wrinkles for frequencies in the range of 100 GHz – 10 THz.

In this paper, we investigate the validity limits of effective material properties of multiphase composites in the context of an EM tissue model. In particular, we discuss the frequency ranges where commonly used homogenized models for these tissue composites based on the effective material theory start deviating from corresponding hierarchical multiscale full-wave EM reference models. We explicitly focus on hypodermal tissues (HYP) as a generic representation of the tissue composite because of their suitably parametrizable morphology, low absorption and high material contrast among intracellular and extracellular constituents. The multiscale modeling of the HYP tissue starts at the smallest length scale with the microstructure of the randomized cell arrangement confined to a computational supercell with dimensions based on the corresponding correlation lengths. This is done in order to grasp the stochastic properties of the underlying composite structure. Our study consists of a systematic two-dimensional (2D) computational EM analysis of HYP tissue surfaces within a generic reflectometry setup for operating frequencies ranging from 10 MHz to 200 GHz. The simulation encompasses 2780 random realizations of HYP tissues for varying structural parameters thus providing a comprehensive Monte-Carlo analysis of the reflectometry scenario. It is worth mentioning that this 2D showcase was only chosen to keep the numerical study manageable within given computer resources. Yet an extension to three dimensions (3D) is straightforward as will be shown in the appendix. The results revealed that, compared to a full-wave analysis of the corresponding cell composites, the validity limits of the homogenized tissue models (EMT) appear at astonishingly low frequencies, typically in the low mm-wave range [19]. This is in contrast to the traditional use of homogenized layer models in tissue analysis/diagnostics [12], [17] and forces any hierarchically organized multiscale model topology to become strongly tied to a corresponding operating frequency bandwidth.

The remainder of the paper is organized as follows: after an introduction into the methodology and implementation of our multiscale EM simulation workbench for the skin reflectometry scenario in Sec. II, we present a comprehensive Monte-Carlo analysis in Sec. III for the validity limits of various homogenized HYP tissues, given by the operating frequencies above which any effective material representation breaks down. In Sec. IV we show that both the lower ''allowed'' frequency band and the upper ''forbidden'' frequency range (where the EMT loses its validity) can be equally exploited for material classification/identification. Using a measure based on the local behavior of the difference between the electric and magnetic energy density we can prove that the spectral fingerprints of the tissues in the forbidden range are particularly apt for predicting features of the tissue's microstructure such as the expected values of cell sizes. The subsequent tissue classification is presented in Sec. V using a machine learning approach based on artificial neural networks (ANN). In addition, we show that ANNs can also be used to identify specific bands in the forbidden frequency range with spectral signatures that can be assigned to specific structural properties of the underlying microstructure, as demonstrated in Sec. V-C. Sec. VI concludes the study by summarizing the main findings and gives an overview of upcoming research. Additional information on classical mixing rules and how they relate to the numerical homogenization procedure implemented in this study is given in Appendix A. In Appendix B, we indicate the transferability of

the research results to three dimensions through corresponding 3D simulations.

II. SIMULATION SETUP AND METHODOLOGY

The numerical study of material composites presented here has two aims. The first aim is to reliably explore the validity limits of their homogenized material representation based on EMT using statistical measures retrieved from a corresponding Monte-Carlo analysis. This implies the numerical analysis of a large number of appropriately parameterized, statistically independent implementations of a given composite. The second aim is to show that the validity limit can be exploited to characterize and classify (bio-)composites. This is performed by looking at signatures in the frequency response of reflected EM waves, which can be attributed to the underlying morphology of the material structures.

To achieve this, a three-stage methodology is applied and implemented in the framework of a multiscale EM simulation workbench whose workflow is shown in Fig. 1.

The methodology starts with Ⓐ an initial homogenization step of the heterogeneous composite using a quasi-static computational EM analysis of a representative composite volume (i.e. the microstructure) yielding the corresponding anisotropic, dispersive EMT representation of the composite. In the next step labelled as Ⓑ the macroscopic effective material properties are then introduced into a computational EM model with a generic reflectometry setup. The focus of this step is on the comparison of the frequency-dependent backscattering from the effective material surface with comparable data from the underlying heterogeneous composite when irradiated by an EM plane wave. A validity limit is then defined as the frequency from which a threshold value in the deviation of the two frequency responses (e.g. 2 %) is exceeded. The last step labelled as Ⓒ encompasses a comprehensive numerical analysis of reflectometry data from large sets of different stochastically generated composites. This type of Monte-Carlo analysis yields reliable statistical measures regarding the validity limits of the underlying effective material representations and is used as the foundation of our material classification with ANNs.

A. RANDOMIZED REPRESENTATION OF THE COMPOSITE MICROSTRUCTURE

In our study we focused on a 2D analysis of HYP as a generic representation of a complex tissue composite. This simplified 2D approach is chosen in order to enable the extensive Monte-Carlo analysis, where an extension to three dimensions (3D) is straightforward as discussed in Appendix B. The 2D representation of the HYP microstructure is depicted in Fig. 2 as a small computational supercell having monodisperse spherical inclusions (i.e. adipose cells) with a diameter $d_{\mathrm{inc}} = 50\ \mu\mathrm{m}$, $\varepsilon_{\mathrm{r},1} = 80$, and $\sigma_1 = 0.53\ \frac{\mathrm{S}}{\mathrm{m}}$ that are embedded in a homogeneous extracellular material with $\varepsilon_{\mathrm{r},2} = 50$, and $\sigma_2 = 0.12\ \frac{\mathrm{S}}{\mathrm{m}}$. The minimum separation distance d_{d} defines the minimum radius around an inclusion where no further adjacent inclusion may be placed. d_{d} is implemented as a dimensionless coefficient greater than 1, which must be multiplied by the inclusion diameter to determine the

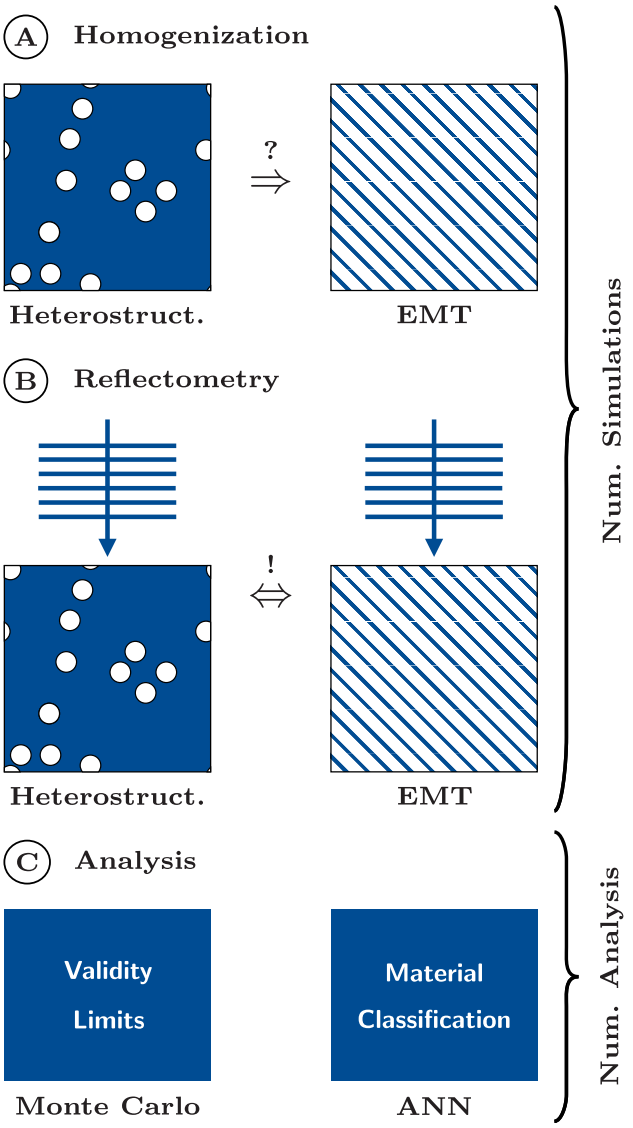

FIGURE 1. Pictogram of the applied methodology. Abbreviations: effective material theory (EMT); artificial neural network (ANN).

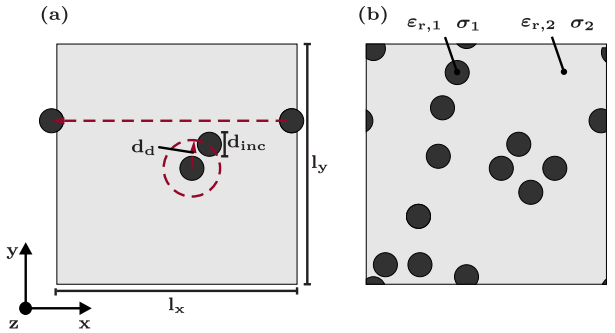

FIGURE 2. Random sequential addition algorithm for the generation of heterogeneous material structures: (a) overview of the adjustable parameters; (b) generic example for a generic parameter setup. In this study: $d_{\mathrm{inc}} = 50\ \mu\mathrm{m}$, $\varepsilon_{\mathrm{r},1} = 80$, $\sigma_1 = 0.53\ \frac{\mathrm{S}}{\mathrm{m}}$, $\varepsilon_{\mathrm{r},2} = 50$ and $\sigma_2 = 0.12\ \frac{\mathrm{S}}{\mathrm{m}}$.

prohibited area around an inclusion. The material parameters remain constant over the entire frequency range, even though the dispersive nature of extracellular and intracellular media would have to be considered for a more realistic tissue representation. The reason for this is a lack of dispersive material parameters in the investigated frequency interval. Thus we considered the parameter estimations provided by [20]. Since the main objective is the evaluation of validity limits in the context of multiscale modelling, the constant material parameters help to ascribe the validity limits more clearly to volume scattering. The implementation of dispersive material parameters to properly consider molecular dispersion, however, would be straightforward using the homogenization procedure proposed in the next subsection.

The dimensions of the computational supercell are $l_x = 1$ mm and $l_y = 1$ mm and chosen accordingly to cover the smallest representative set of inclusions for a given volume fraction $c_v = \frac{V_{inc}}{V_{supercell}}$. In order to mimic a realistic HYP microstructure, a stochastic representation of the supercell is chosen. In this, the placement of the inclusions is automatically performed by the random sequential addition (RSA) algorithm [21] for a given volume fraction c_v and a distance parameter d_d to omit touching and merging of inclusions. The algorithm is modified to enable the periodic continuation of the supercell according to corresponding periodic boundary conditions as illustrated in Fig. 3, which reduces the later numerical backscattering analysis to a single supercell.

B. HOMOGENIZATION

For the homogenization, the 2D supercell containing the heterogenous 2D microstructure of the tissue composite (cf. Fig. 2(b)) is placed into an idealized parallel plate capacitor setup. As depicted in Fig. 3, a time-harmonic voltage with constant amplitude $\hat{\underline{u}} = \underline{\varphi}_1 - \underline{\varphi}_2$ is applied between two opposing supercell edges that are designed as electrodes (i.e Dirichlet boundary conditions).

The two remaining edges are defined as periodic boundary conditions (PBC) in order to suppress fringing fields and to reduce the memory resources of the subsequent quasi-static EM simulation. This approach, which has been implemented with different boundary conditions, has been used in the past to investigate and quantify the influence of interfacial polarization (Maxwell-Wagner) in composite materials compared to calculations based on classical mixing rules [22]. A detailed comment on how these mixing rules may be associated to our estimation of validity limits based on numerical multiscale analysis is elucidated in Appendix A. In order to cope with the anisotropy of the underlying microstructure the supercell is then excited in the other (orthogonal) direction while swapping the electrodes with the PBCs (and vice versa) as shown in Fig. 3. The capacitor setup is implemented in the finite-element-method-based (FEM) software package COMSOL Multiphysics [23]. Each 2D simulation model can therefore be interpreted as an infinitely extended 3D capacitor of finite thickness due to two extensions, namely in the

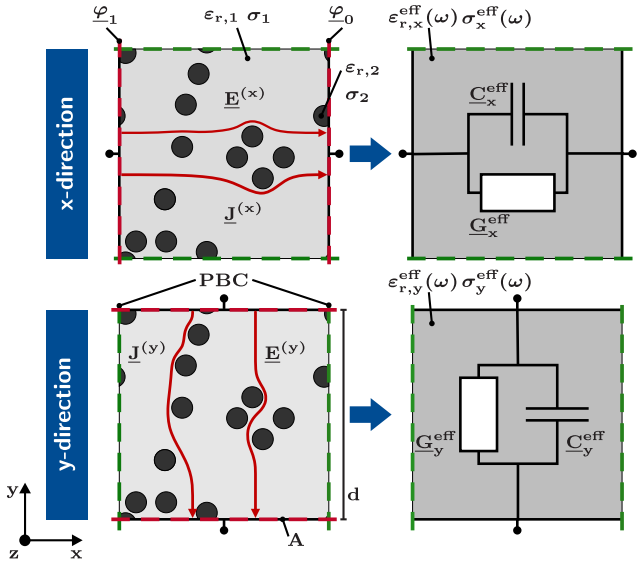

FIGURE 3. Schematic of the homogenization procedure: For the tensorial acquisition of the material parameters, the effective material properties are determined successively with respect to the individual spatial directions.

direction of the periodic continuation and along the translationally invariant direction normal to the 2D plane. From the time-harmonic quasi-static EM analysis of the supercell in the form of the capacitor setup, an effective admittance is retrieved that is represented by the equivalent electrical parallel circuit consisting of the elements G^{eff} and C^{eff}. This is given by

$$\underline{Y}^{eff}(\omega) = \frac{\hat{\underline{i}}(\omega)}{\hat{\underline{u}}} = G^{eff}(\omega) + j\omega C^{eff}(\omega). \tag{1}$$

where the applied voltage $\hat{\underline{u}}$ and the resulting current $\hat{\underline{i}}(\omega)$ are directly accessible via COMSOL Multiphysics. The effective material properties ε^{eff} and σ^{eff} are thus easily deduced according to

$$\underline{Y}^{eff}(\omega)\frac{d}{A} = \frac{\hat{\underline{i}}(\omega)}{\hat{\underline{u}}} \cdot \frac{d}{A} = \underbrace{\sigma^{eff}(\omega) + j\omega\varepsilon_0\varepsilon_r^{eff}(\omega)}_{\underline{\sigma}^{eff}(\omega)} \tag{2}$$

where d is the parallel plate distance and A stands for the area of the electrode. In Eq. 2, the right-hand term can be interpreted as the complex effective conductivity $\underline{\sigma}^{eff}(\omega)$ of the homogenized effective material from which the required material parameters directly follow:

$$\sigma^{eff}(\omega) = \Re\{\underline{\sigma}^{eff}\} \tag{3}$$

and

$$\varepsilon_r^{eff}(\omega) = \frac{\Im\{\underline{\sigma}^{eff}\}}{\omega\varepsilon_0}. \tag{4}$$

In order to consider anisotropies in the effective material the quasi-static capacitor analysis is performed with excitation in both the x and y-directions (cf. Fig. 3) yielding corresponding frequency-dependent second-rank tensors for the effective permittivity and effective conductivity, respectively.

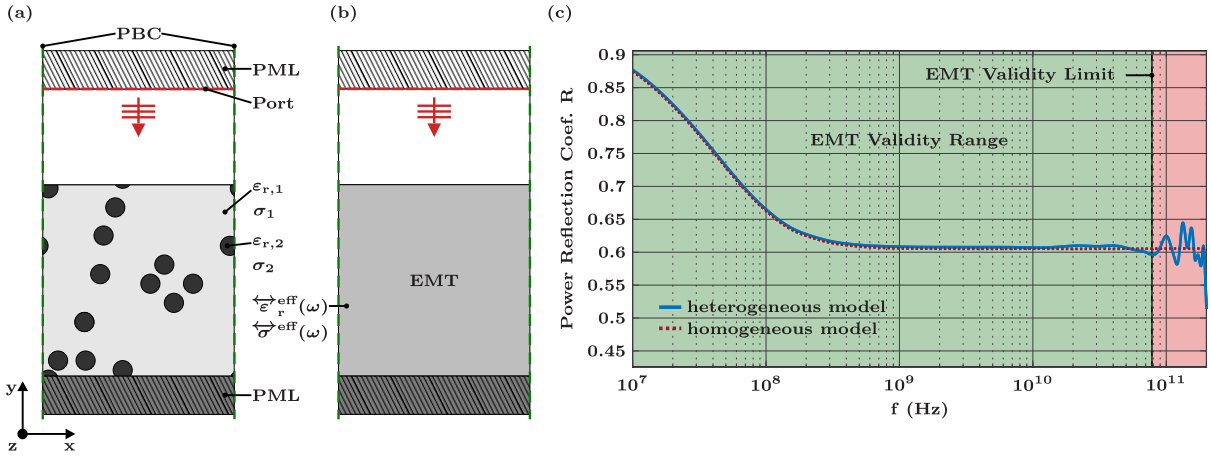

FIGURE 4. Comparison between the heterogeneous and homogenized (EMT) model of a generic HYP model: (a) heterogeneous simulation setup; (b) homogeneous simulation setup; (c) spectral responses of the reflectance (showing the typical Maxwell-Wagner roll-off in the MHz range) for $\varepsilon_{r,1} = 80$, $\sigma_1 = 0.53\ \frac{S}{m}$, $\varepsilon_{r,2} = 50$, $\sigma_2 = 0.12\ \frac{S}{m}$, $d_{inc} = 50\ \mu$m, and $c_v = 0.452$.

For the conductivity

$$\overleftrightarrow{\sigma}^{\text{eff}}(\omega) = \begin{pmatrix} \sigma_x^{\text{eff}}(\omega) & 0 \\ 0 & \sigma_y^{\text{eff}}(\omega) \end{pmatrix} \tag{5}$$

and for the permittivity

$$\overleftrightarrow{\varepsilon}_r^{\text{eff}}(\omega) = \begin{pmatrix} \varepsilon_{r,x}^{\text{eff}}(\omega) & 0 \\ 0 & \varepsilon_{r,y}^{\text{eff}}(\omega) \end{pmatrix}. \tag{6}$$

These are the homogenized, frequency-dependent effective material representations that are later introduced (in accordance with the multiscale-modeling approach) into the simulation model of the generic reflectometry setup.

C. REFLECTOMETRY

The generic reflectometry setup is used to analyze the reflection of an impinging EM plane wave from a surface system that is defined by a plane boundary between air and either a heterogeneous composite material or its homogenized EMT representation (cf. Fig. 4). The plane wave is excited from a non-reflective port under the angle of incidence α_{inc} (here 0 °) having either s or p-polarization with respect to the reflection plane (i.e. x-y plane). The amplitude of the incident plane wave is assigned to a constant input power P_0 whereas the reflected power P_R is detected by the same non-reflective port from which the desired measure, namely the power reflection coefficient $R = \frac{P_R}{P_0}$, is calculated. The absorption coefficient $A = \frac{P_A}{P_0}$ is determined by a corresponding volume integration of the material losses P_A within the material structure. The top and bottom of the computational domain are terminated with perfectly matched layers (PML), which are assigned the effective material parameters defined by $\overleftrightarrow{\varepsilon}_r^{\text{eff}}(\omega)$ and $\overleftrightarrow{\sigma}^{\text{eff}}(\omega)$ and the material parameters of the air respectively. Similar to the capacitor setup, PBCs are also introduced into the reflectometry model to omit fringing fields while extending the randomized super cell to a periodic representation of the composite surface layer.

A first example for analyzing the breakdown of the effective material representation is given in Fig. 4(c) for HYP tissue with a cell volume fraction of $c_v = 0.45$. The simulation has been performed on a PC equipped with an Intel i7-6700k processor (4 cores) and 64 GB DDR4 RAM. In the given frequency interval, 260 frequency points have been simulated with a MUMPS solver where the density of the frequency points increases for higher frequencies. The increasing density can be interpreted as a frequency-dependent sampling rate to cover interference patterns within the forbidden range correctly. The simulation for each frequency point lasts 21 s and includes the simulation of the heterogeneous microstructure and its homogenized representation in s and p-polarization. The blue curve represents the power reflection coefficient of the heterogeneous composite model and the dotted red curve that of the homogeneous EMT model for p-polarized excitation in a frequency range from 10 MHz to 200 GHz. Since in s-polarization the electric field points in the translation-invariant direction of the composite and therefore homogenization is not defined, the comparison between the reflectance of the heterogeneous material structure and its homogenized representation is only done for p-polarization. The validity limit of the EMT representation for a deviation of 2 % between the two frequency responses is located at $f_{\text{val}} = 78$ GHz for this particular HYP tissue realization. The validity range of the homogenized EMT representation therefore extends below the validity limit. However, the forbidden range found above this limit is characterized by strong variations in the frequency response. These are associated with the heterogenous tissue model which defines a characteristic fingerprint which can be exploited for material classification.

III. MONTE-CARLO ANALYSIS OF VALIDITY LIMITS

Since the analysis of a single HYP tissue structure has only minor significance for the reliable determination of the associated EMT representation's validity limit, the

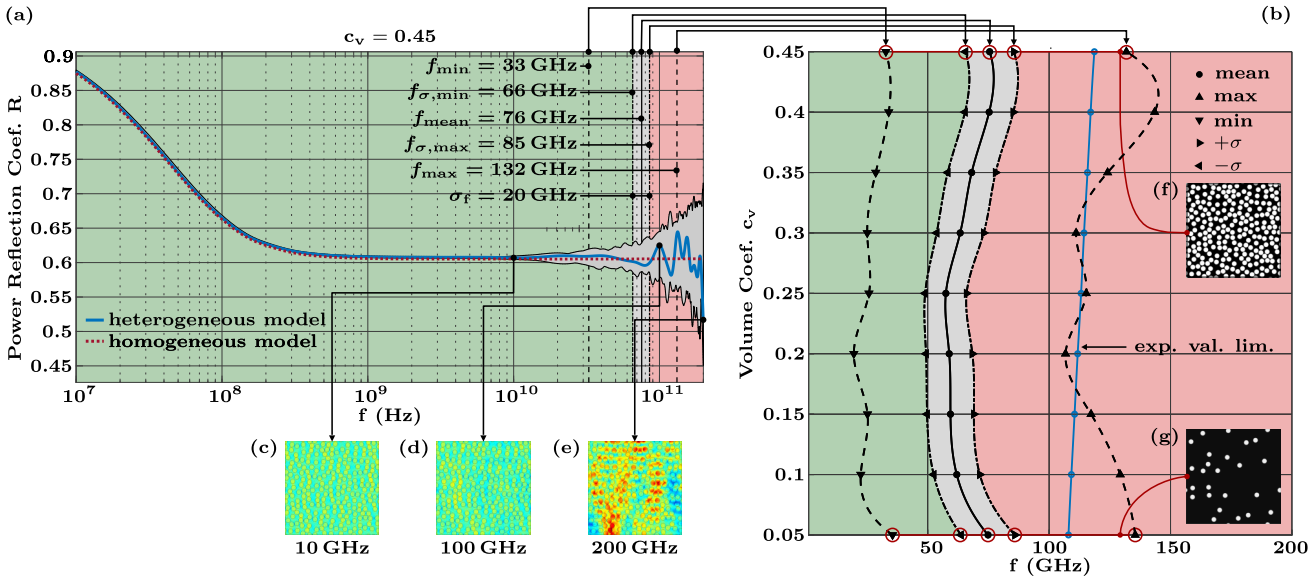

FIGURE 5. Validity limits for several generic HYP derivatives: (a) spectral responses of the reflectance (showing the typical Maxwell-Wagner roll-off in the MHz range) of 220 implementations (for $\varepsilon_{r,1} = 80$; $\sigma_1 = 0.53$ S/m; $\varepsilon_{r,2} = 50$; $\sigma_2 = 0.12$ S/m; $d_{inc} = 50\ \mu$m; and volume fraction $c_v = 0.45$); (b) Validity limits of the derivatives of a heterogeneous material structure (here the HYP tissue), the blue line indicates the expected validity limit based on classical considerations; (c), (d), (e) examples of the electric field distribution $|\underline{\tilde{E}}|$ at various frequencies (i.e. at 10 GHz, 100 GHz, 200 GHz, respectively); (f), (g) examples of the analyzed microstructures (i.e. for $c_v = 0.45$ and $c_v = 0.05$ respectively). The validity range of the EMT material model is colored in green while the forbidden range is marked red.

procedure presented in Sec. II is thus performed for a large number of randomly generated realizations of the same HYP tissue based on a corresponding structural parameter set labelled as P_i. Each set P_i contains fixed values for both the minimal separation distance $d_d = 1.05$ and the diameter $d_{inc} = 0.05$ mm of the HYP's spherical inclusions together with a specific volume fraction $c_{v,i} \in \{0.05, 0.1, \ldots, 0.45\}$. In this sense, 9 different HYP tissue types are addressed corresponding to the parameter sets $P_1, \ldots, P_9$ with altered volume fractions $c_{v,1}, \ldots, c_{v,9}$ (cf. Table 1). Within the framework of a Monte-Carlo analysis 220, statistically independent microstructures with randomly distributed inclusions were created for each P_i and corresponding $c_{v,i}$. These are considered in the following as realizations of the parameter set P_i. Examples of such microstructures are shown in Fig. 5(f) and 5(g) for the parameter sets $P_9 := (d_d = 1.05, d_{inc} = 0.05, c_v = 0.45)$ and $P_1 := (d_d = 1.05, d_{inc} = 0.05, c_v = 0.05)$ respectively. As an example, the statistical analysis for the HYP sample P_9 ($c_v = 0.45$) with 220 randomly generated realizations of the heterogeneous composite is illustrated in Fig 5(a). The frequency responses of the simulated power reflection coefficient of all realizations are confined to the gray shaded area between the top and bottom envelope, with the blue curve labeling a single representation of this spectral set which has already been depicted in Fig. 4(c). The red-dotted curve shows the performance of the HYP tissues' homogenized EMT model. The validity limits of the EMT homogenization are determined as the frequency above which the power reflection of the homogeneous EMT model and the heterogeneous composite model deviate by more than 2 %. For the example of P_9,

TABLE 1. Overview of the material and structural parameters of parameter sets P_1 to P_9.

$\varepsilon_{r,1} = 80$; $\sigma_1 = 0.53$ S/m; $\varepsilon_{r,2} = 50$; $\sigma_2 = 0.12$ S/m				
260 sampled frequency points (10 MHz to 200 GHz)				
P_i	d_d	d_{inc}	c_v	realizations
P_1	1.05	0.05 mm	0.05	220
P_2	1.05	0.05 mm	0.1	220
P_3	1.05	0.05 mm	0.15	220
P_4	1.05	0.05 mm	0.2	220
P_5	1.05	0.05 mm	0.25	220
P_6	1.05	0.05 mm	0.3	220
P_7	1.05	0.05 mm	0.35	220
P_8	1.05	0.05 mm	0.4	220
P_9	1.05	0.05 mm	0.45	220

this yields a corresponding data set of 220 values with a mean frequency $f_{mean} = 76$ GHz, which in the following is defined as the representative value for the validity limit. The associated standard deviation is $\sigma_f = 20$ GHz leading to a first upper and lower bound of $f_{\sigma,min} = 66$ GHz and $f_{\sigma,max} = 86$ GHz whereas an absolute minimum and maximum of this limit corresponds to $f_{min} = 33$ GHz and $f_{max} = 132$ GHz as depicted in Fig. 5(a). The validity range of the EMT material model is colored in green while the forbidden range, in which the EMT representation breaks down, is marked red. In the following, the overall Monte-Carlo analysis has been carried out for all parameter sets $P_1, \ldots, P_9$ and their respective volume fractions $c_{v,1}, \ldots, c_{v,9}$ (cf. Fig. 5(b)). This revealed validity limits for HYP tissues at astonishingly low frequencies around $60 - 80$ GHz. The classical estimation of validity limits according to EMT [24] by means

of $\frac{\lambda_m}{2\pi} > d_{inc}$, where λ_m denotes the wavelength within the material, is significantly higher between 110 GHz and 120 GHz (see Fig. 5(b) blue line). This is an interesting result as it may challenge assumptions made in commonly used tissue models for mm-wave [12] and THz frequencies [11]. In addition, the statistical evaluation of all parameter sets has also led to validity limits with only weak dependence on the volume fraction of the lipid droplets (i.e. inclusions) in the adipose HYP tissue. Fig. 5(c)-(e) depict the electric field distributions $|\vec{\underline{E}}|$ within the microstructure of the heterogeneous composite for three distinct frequencies along the blue curve. As expected from EMT, these field profiles are quite homogeneous at frequencies in the validity range (e.g. 10 GHz), but display interference patterns at forbidden frequencies (e.g. 100 GHz and 200 GHz) with emerging spatial correlations to the underlying microstructure. In the context of reflectometry-based tissue characterization, these correlations will establish the possibility of using spectral fingerprints in the forbidden range, shown, for example, by the blue curve in Fig. 5(a), to classify microscopic features of the heterogeneous microstructure. In contrast, the well-behaved frequency response in the validity range allows for the extraction of macroscopic quantities such as the underlying volume fraction of the inclusions. This will be discussed in the next section.

IV. ON THE INFORMATION CONTENT OF THE FORBIDDEN FREQUENCY BAND

The existence of validity limits has direct consequences on the use of EMT-based multiscale models for multi-layered tissue systems such as skin. In such models the maximum frequency is determined by the tissue layer with the lowest validity limit, thus yielding an allowed operating frequency band which becomes specific to the overall skin model. At higher frequencies outside this band, the described homogenization of the particular tissue layer is not applicable anymore and its further analysis requires an accurate modelling of its proper microstructure, which actually leads to a modified multiscale skin model. An ultra-broadband tissue analysis must therefore consider simultaneous structural changes in the tissue models during the frequency-domain simulation while relying on an appropriately prepared set of multiple model representations. These multiple representations can be set up prior to numerical analysis, e.g. when using machine learning-based predictions of the validity limits involved.

As indicated in the previous section the increasing impact of the microscopic properties on the frequency response beyond the validity limit opens up the possibility to identify and classify specific features of the tissue's microstructures based solely on the associated spectral fingerprint in the forbidden frequency range. This reasoning can be underpinned by correlating characteristic features in this spectral fingerprint with emerging interference patterns in the microstructure. In an illustrative example, we studied specific frequency points in the spectral fingerprints of the power reflection R and absorption A between 100 GHz and 200 GHz for a single HYP tissue realization ($c_v = 0.45$) in conjunction with the associated EM field patterns in the microstructure.

A field quantity of particular significance here is the difference between electric and magnetic energy density Δw. This measure has already proven successful in the assessment of advanced MRI coils [25]. It is derived from the time-harmonic version of the Poynting theorem, represents for the conservation of the EM energy flux $\vec{\underline{S}}$ (i.e. the Poynting vector) as shown in Eq. (7) where $\vec{\underline{S}}$ has to fuel areas with dissipation loss and at the same time to compensate for temporal changes in the reactive power.

$$\nabla \cdot \vec{\underline{S}} = -\underbrace{\frac{1}{2}\sigma|\vec{\underline{E}}|^2}_{p} - j2\omega \underbrace{\frac{1}{4}\left(\mu|\vec{\underline{H}}|^2 - \varepsilon_0\varepsilon_r|\vec{\underline{E}}|^2\right)}_{\Delta w = w_m - w_e}, \quad (7)$$

The reactive power term contains the difference Δw between the electric and magnetic energy density where Δw emerges only if the energy density distributions of both field quantities are spatially separated. The quantity Δw thus indicates a locally confined resonant enhancement of reactive fields in the tissue's very microstructure while also highlighting potential "hot spots" in the loss density p. This is mainly due to oscillating balancing currents between these separated energy densities. The dissipated power P_A in the tissue results from integrating the power loss density p over the tissue volume yielding the absorption A.

Applied to the proper heterogeneous material representation of an illustrative HYP realization, Eq. 7, and its derived measures, can be used to investigate correlations between the spatial field distribution within the microstructure and the spectral fingerprint in the forbidden range. In this case, the local electric and magnetic field strengths, $\vec{\underline{E}}(\vec{r}) = (E_x(\vec{r})\ E_y(\vec{r})\ E_z(\vec{r}))^T$ and $\vec{\underline{H}}(\vec{r}) = (H_x(\vec{r})\ H_y(\vec{r})\ H_z(\vec{r}))^T$ respectively, are used for calculation, where $\vec{r}$ denotes the spatial position. As depicted in Fig. 6, Δw provides the most selective map of the resonant loss enhancement which is highly correlated to the tissue's microstructure and thus to the randomized HYP cell distribution. With this connection between microstructure affine field patterns and specific signatures in the spectral fingerprint, we reason that the spectral responses in the forbidden frequency range contain enough information for the characterization of the underlying microstructure. In the following, the spectral responses of both power reflection R and absorption A of the given HYP tissue are plotted in Fig. 7 for the previously mentioned region of interest in the forbidden frequency range. Apart from the expected opposing behavior of the frequency responses of R and A [cf. Fig. 7(a) and (b)] where a reflection maximum is accompanied by an absorption minimum, there are distinct subintervals demonstrating different behavior, such as that between 184 GHz and 188 GHz (shaded gray). An enlarged view of this specific region is plotted in Fig. 7(c) and 7(d) and shows both R and A forming unique spectral substructures. In the following we analyzed local extrema at frequencies 160.7 GHz, 187.1 GHz, 187.9 GHz and 190.3 GHz outside and within the sub-interval (labelled by red dots).

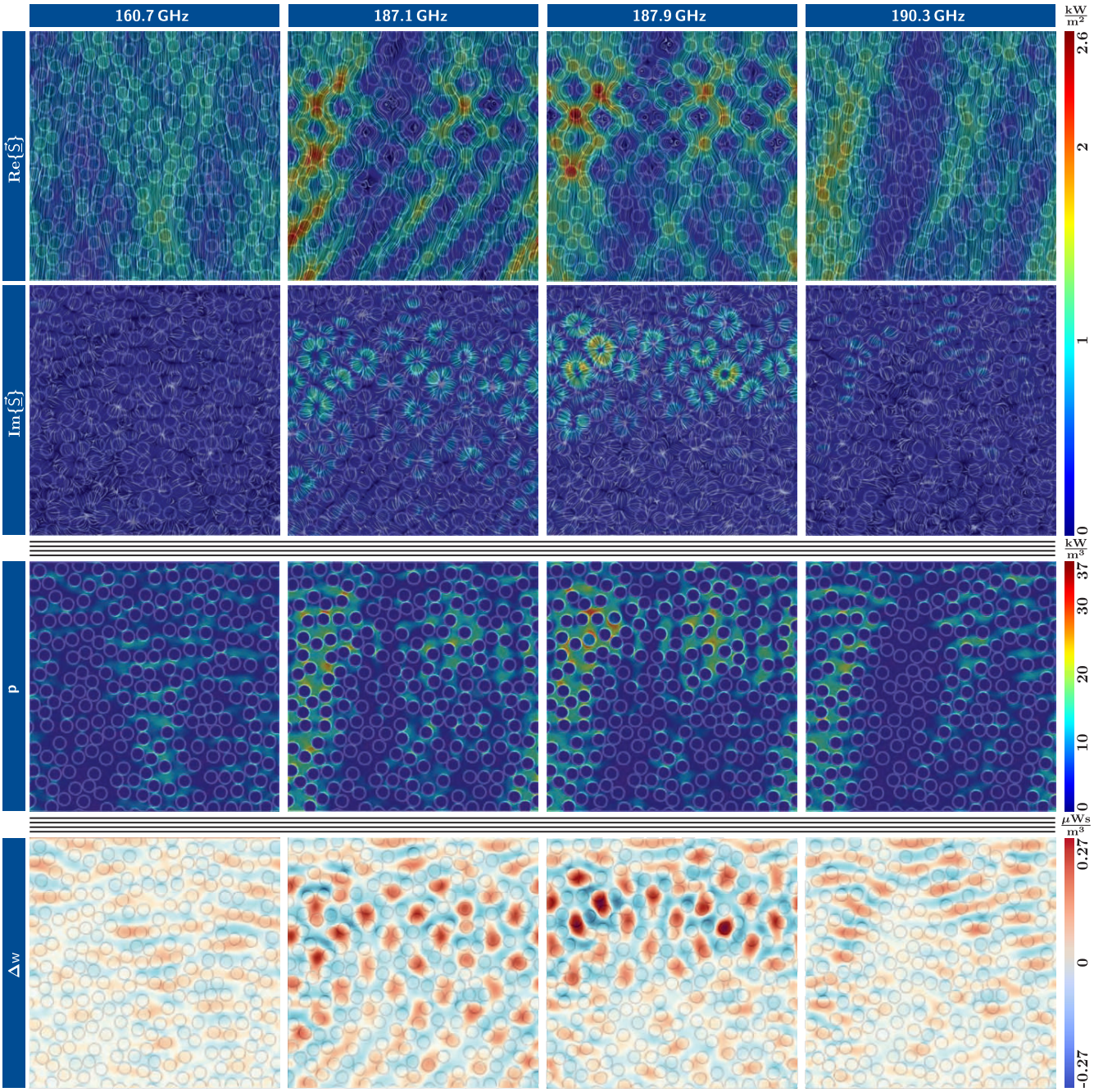

FIGURE 6. Graphical evaluation of the EM fields within the microstructure for the frequency points 160.7 GHz, 187.1 GHz, 187.9 GHz and 190.3 GHz (i.e. for $\varepsilon_{r,1} = 80$; $\sigma_1 = 0.53$ S/m; $\varepsilon_{r,2} = 50$; $\sigma_2 = 0.12$ S/m; $d_{inc} = 50$ μm; and volume fraction $c_v = 0.45$). From the top to the bottom row: the real part of the Poynting vector Re$\{\underline{\vec{S}}\}$, the imaginary part Im$\{\underline{\vec{S}}\}$, the loss density p, and the difference of enegery densities Δw.

The associated field patterns regarding flowing, dissipating and stored energy are depicted in Fig. 6 partly using a generalized field line representation provided by the line integral convolution (LIC) method [26]. Comparing these fields inside the subinterval (at 187.1 GHz and 187.9 GHz) with those outside (at 160.7 GHz and 190.3 GHz) indicates that the imaginary part of the energy flux $\underline{\vec{S}}$ yields the most distinct correlations to the underlying microstructure. This is even more distinct when using Δw, which is actually derived from Im$\{\underline{\vec{S}}\}$. We can therefore assume that these unique spectral substructures in the spectral responses may, in particular, significantly contribute to the information content about the tissue's microstructure. This makes it easy to understand that promising tissue characterization schemes based on skin surface reflectometry could implicitly use such unique spectral features and eventually exploit them in the framework of a supervised learning-based classification approach. In the following section we therefore present a successful procedure

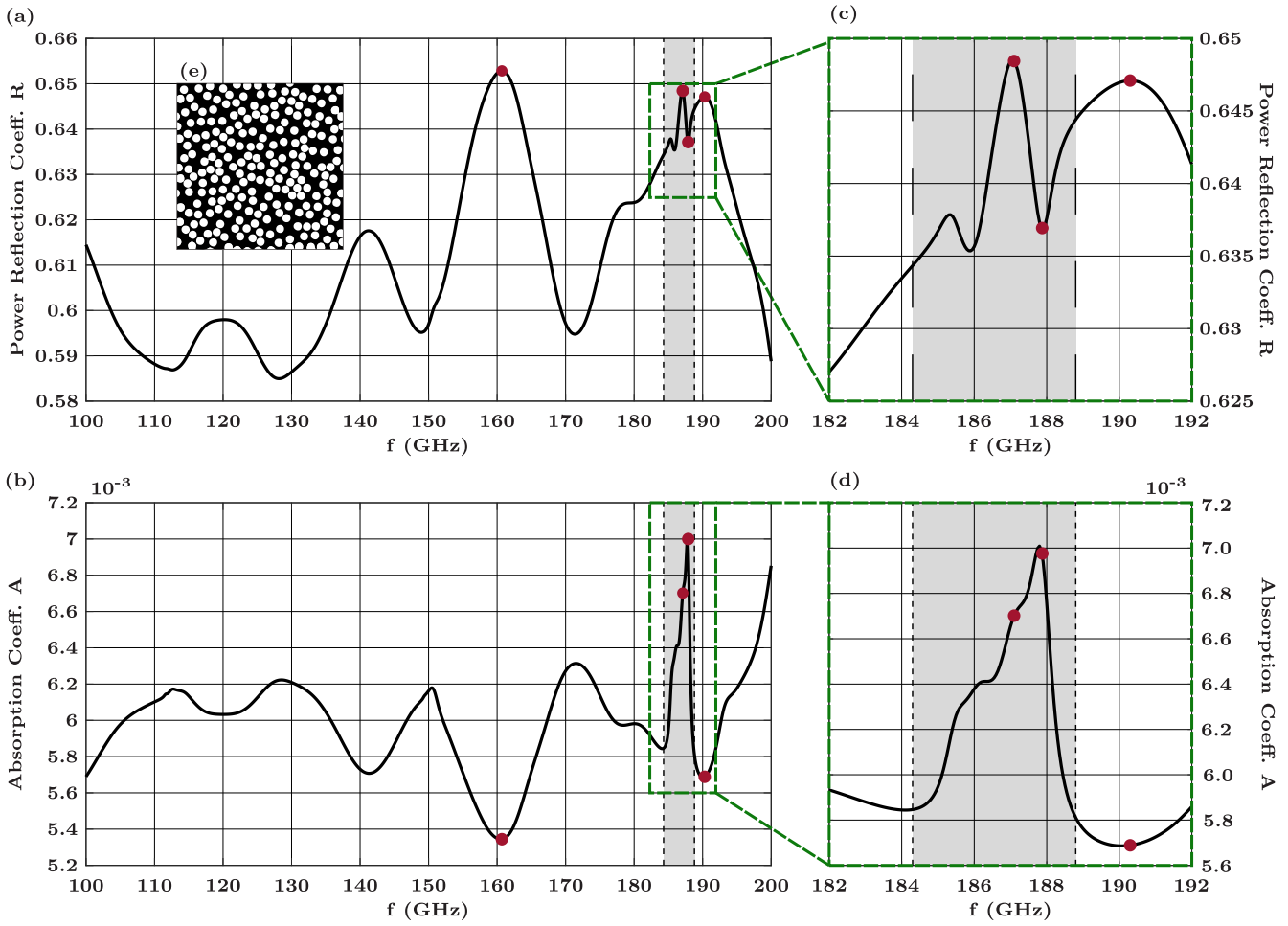

FIGURE 7. Spectral response in the forbidden frequency range between 100 GHz and 200 GHz: (a) reflectance; (b) absorptance; (c), (d) detailed enlargements of the reflectance and absorptance in the subinterval between 182 GHz and 188 GHz; (e) example of the analysed HYP realization (i.e. for $\varepsilon_{r,1} = 80$; $\sigma_1 = 0.53$ S/m; $\varepsilon_{r,2} = 50$; $\sigma_2 = 0.12$ S/m; $d_{inc} = 50$ μm; and volume fraction $c_v = 0.45$).

that utilizes the spectral fingerprints of the HYP structures in both the valid and the forbidden frequency range for reflectometry-based tissue classification with ANN.

V. ANN-BASED TISSUE CLASSIFICATION

Based on the relationship between the resonances in the underlying microstructure and interference patterns in the spectral response of the reflection coefficient, we are going to present an academic case study to demonstrate the existence of spectral subintervals bearing information about specific morphological features. For this purpose, we extended the Monte-Carlo analysis by including parameter sets with variable structural parameters for the inclusion diameter and the volume fraction of the lipid droplets. Then we identified the resulting HYP derivatives with a image recognition-based material classification procedure using ANN. With this classification we will demonstrate the existence of spectral subintervals bearing information about specific morphological features. For this reason the remainder of this section is as follows. In the first subsection, we will show that the valid and the forbidden frequency ranges complemented each other with regard to the information content contained in the spectral fingerprint. In the second subsection, we will show that the forbidden frequency range could be exploited to predict the microstructure of the HYP tissues (e.g. the expectation values of the cell sizes) and the validity range in order to classify aggregated HYP tissue properties such as the volume fractions of the adipose cells. In the last subsection, we will describe a method developed here based on occlusion sensitivity to identify and subsequently select information-carrying frequency ranges which can be correlated to specific structural properties of the microstructure.

A. DATA SETS FOR MICROSTRUCTURE CLASSIFICATION

For the tissue classification based on ANN we have exploited both the forbidden frequency range to predict the microstructure of the HYP tissues (e.g. the expectation values of the cell sizes) and the validity range to classify aggregated HYP tissue properties such as the volume fractions of the adipose cells. In this regard the Monte-Carlo analysis described in Sec. III is

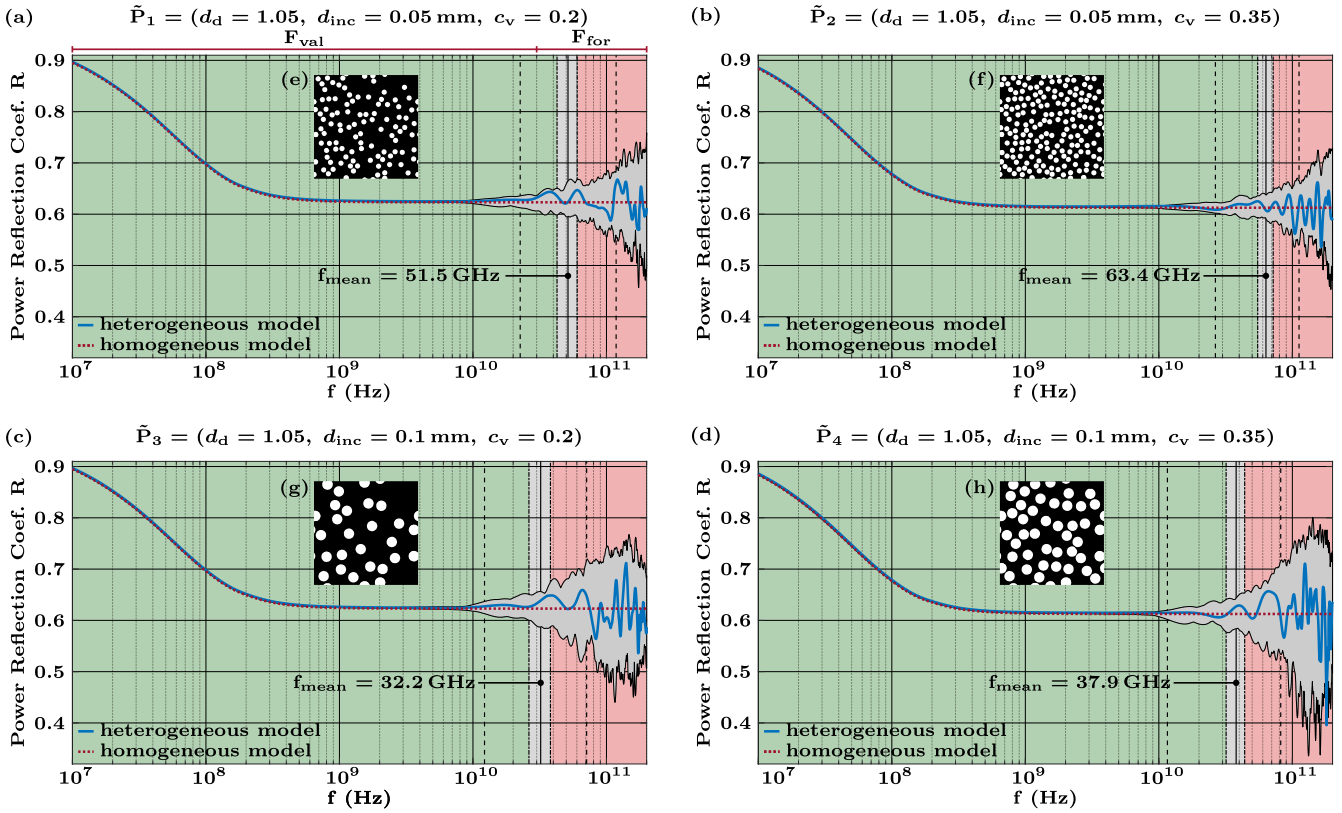

FIGURE 8. Overview of the parameter sets $\tilde{P}_1$ to $\tilde{P}_4$: (a)-(d) spectral responses of the reflectance of 200 statistically independent HYP realizations of the individual parameter sets; (e)-(h) examples of the analysed microstructures.

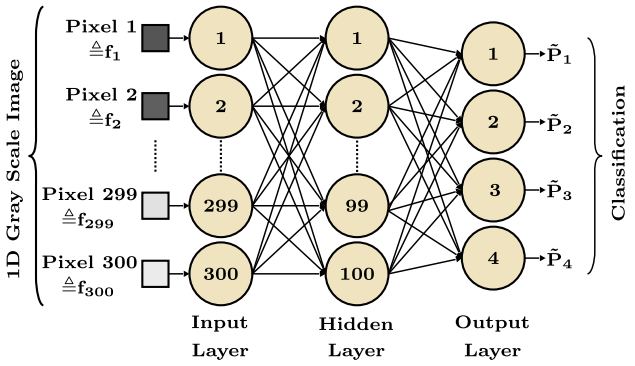

FIGURE 9. Overview of the network architecture: A 1D-image input layer for the processing of 300 image pixels consisting of 300 neurons, a subsequent fully connected hidden layer with 100 neurons which has a rectified linear unit (ReLU) activation function followed by a fully-connected output classification layer (using a softmax function) in which the number of neurons is derived from the number of categories to be classified ($\tilde{P}_1$ to $\tilde{P}_4$).

TABLE 2. Overview of the material and structural parameters of parameter set $\tilde{P}_1$ to $\tilde{P}_4$.

$\varepsilon_{r,1} = 80$; $\sigma_1 = 0.53\,S/m$; $\varepsilon_{r,2} = 50$; $\sigma_2 = 0.12\,S/m$				
260 sampled frequency points (10 MHz to 200 GHz)				
$\tilde{P}_i$	d_d	d_{inc}	c_v	realizations
$\tilde{P}_1$	1.05	0.05 mm	0.2	200
$\tilde{P}_2$	1.05	0.05 mm	0.35	200
$\tilde{P}_3$	1.05	0.1 mm	0.2	200
$\tilde{P}_4$	1.05	0.1 mm	0.35	200

extended by four additional parameter sets $\tilde{P}_1$ to $\tilde{P}_4$ with fixed values for $d_d = 1.05$ and variable structural parameters for $d_{inc} \in \{0.05\,mm, 0.1\,mm\}$ and $c_v \in \{0.2, 0.35\}$ (cf. Table 2). The reflectometry data of these four generic HYP tissues is given in Fig. 8, where each of them is numerically represented by 200 statistically independent realizations of the underlying microstructure. To investigate the performance of the classification procedure, the analyzed spectral range is subdivided into 2 frequency intervals F_{val} and F_{for} as depicted in Fig. 8(a). The interval $F_{val} := [10\,MHz; 30\,GHz]$ covers the characteristic Maxwell-Wagner roll-off associated with the relaxation effects of polarization charges at the cell surface. $F_{for} := [30\,GHz; 200\,GHz]$ includes the range of the proper validity limit and the forbidden frequency range.

In preparation for ANN-based classification, the spectral fingerprint of each randomized realization is sampled at 300 discrete frequency points within the complete frequency range as well as in each of the given subintervals F_{val} and F_{for}. The 300 discrete frequency points are determined by interpolating the 260 frequency points simulated for each realization (cf. Sec. II-C). The sampled values of the power reflection are displayed according to a grayscale coding.

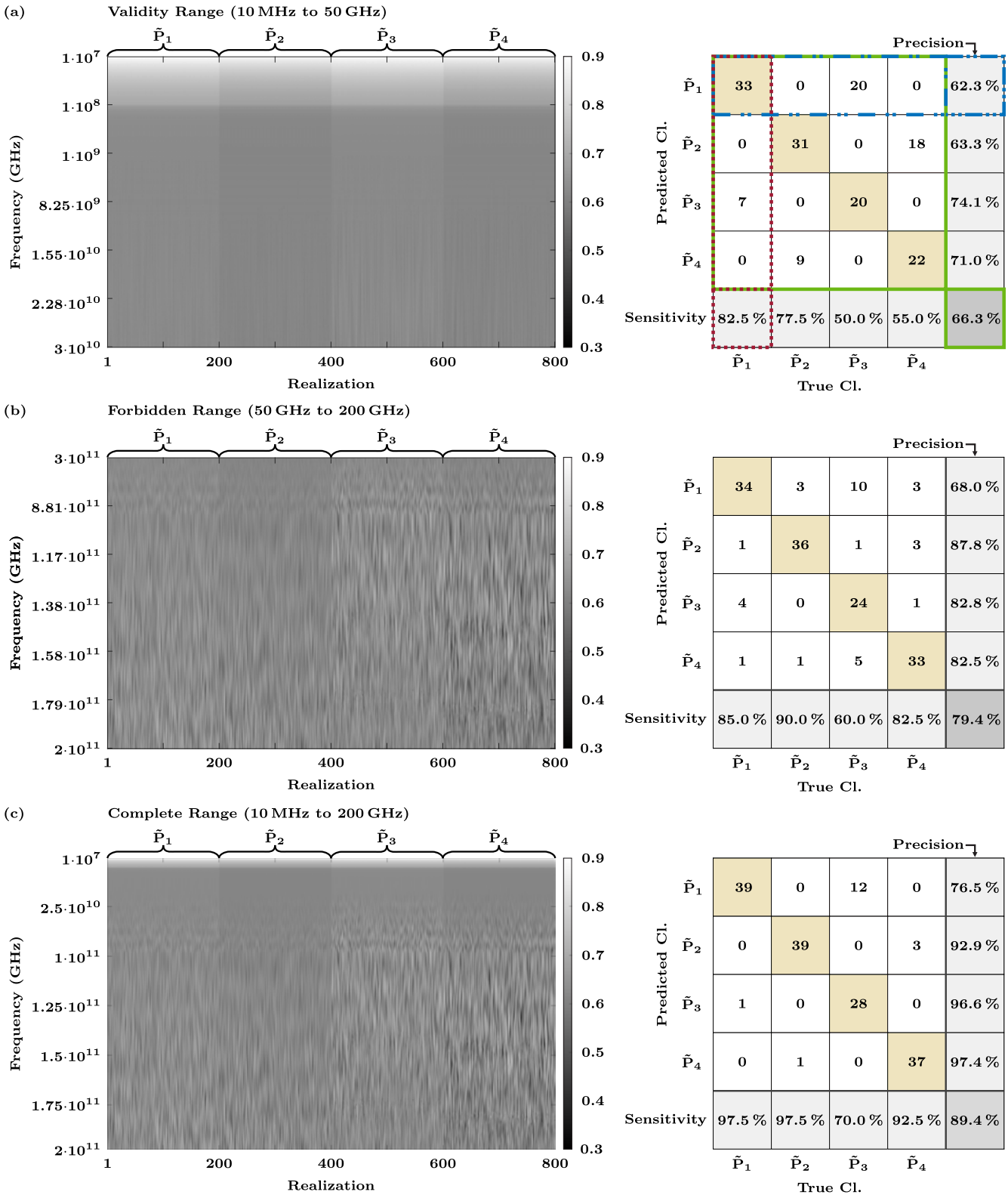

FIGURE 10. Overview of the ANN-based classification of 4 generic tissue derivatives represented by the parameter sets $\tilde{P}_1$ to $\tilde{P}_4$ using the spectral fingerprint in the validity, forbidden and complete frequency range summarized in confusion matrices in (a) to (c), respectively. The corresponding grayscale images display the reflection coefficient of each realization of the considered parameter sets sampled at 300 discrete frequency points in a grayscale coding.

The resulting data set, encompassing the realizations of the corresponding frequency interval, can therefore be depicted as a 2D grayscale image with 300 image pixels along the frequency axis and the corresponding label indices of the spectral fingerprints along the other dimension.

The resulting image recognition-based material classification is implemented by the use of shallow ANNs as depicted in Fig. 9 and performed with the image processing library of the MATLAB programming environment (version R2018a). The ANNs consist of a 1D-image input layer for the 300 image pixels consisting of 300 neurons, a subsequent fully connected hidden layer with 100 neurons which has a rectified linear unit (ReLU) activation function followed by a fully-connected output classification layer (using a softmax function) in which the number of neurons is derived from the number of categories to be classified (in this case 4 classes referring to the parameter sets $\tilde{P}_1$ to $\tilde{P}_4$ depicted in Fig. 8). As a training scheme, the stochastic gradient descent with momentum (SGDM) method was applied to 80 % of the available data where every network was trained over 3000 epochs yielding an overall training time of approximately 5 minutes. For comparability of the classification results, the network architecture (cf. Fig.9) was used for all frequency intervals. The remaining 20 % of the data was used to test the trained ANNs' performance.

The results of the classification in the validity and the forbidden range as well as in the complete frequency range are depicted in Fig. 10(a) to (c) respectively. In these, the spectral fingerprints of all 800 realizations are plotted according to the mentioned grayscale coding and represent the input data for the ANNs. The results of the ANN-based classifications are summarized in the corresponding confusion matrices (test set data). These confusion matrices compare the classes of the individual realizations predicted by the ANN against their actual classes. The correctly assigned realizations are arranged on the main diagonals of the matrices and the incorrectly assigned ones on the minor diagonals. The overall performance of the classification is evaluated by three metrics, namely *accuracy*, *precision* and *sensitivity*. The *accuracy* (green frame Fig. 10(a)), which can be regarded as the overall quality measure of the classification, is calculated as the ratio of correct predictions to all predictions of a classification. The *precision* (blue frame) is calculated as the ratio of the correct predictions to all predictions within a particular class. The *sensitivity* (red frame) is calculated as the ratio of the correct predictions to all actual elements of a particular class.

The lowest accuracy is achieved with 66.3 % in the validity range. If the data from the forbidden range is used, the accuracy improves to 79.4 %. This shows that within the forbidden range there is a high information content for the classification of microstructures. However, if the entire spectrum is used for classification, an accuracy of 89.4 % can be achieved. This implies that the information content of both ranges is complementary and makes the classification more reliable.

In order to investigate the extent to which the validity and the forbidden range complement each other, we will examine whether specific properties of the microstructure can be classified in specific frequency ranges in the following subsection.

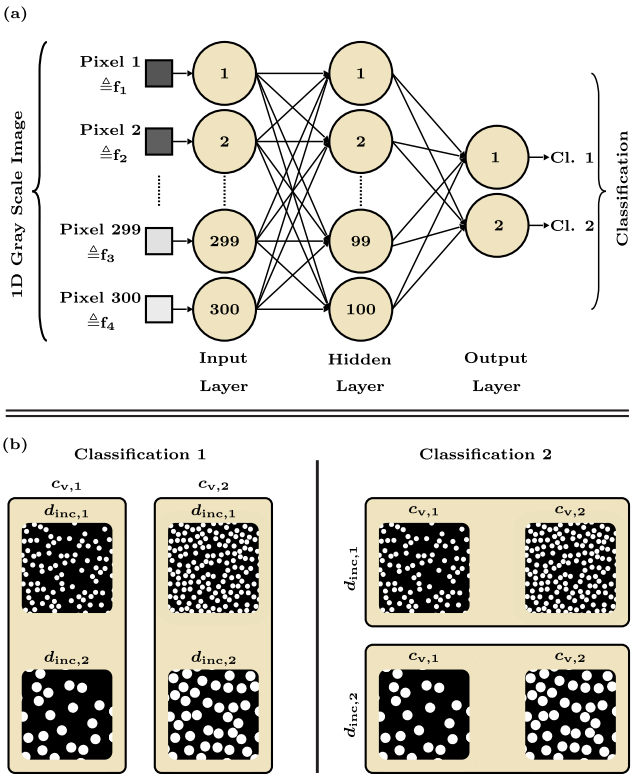

FIGURE 11. Implemented modifications for the binary classification: (a) Reduction of the output layer to two neurons. (b) Reorganization of the parameter sets $\tilde{P}_1$ to $\tilde{P}_4$ into two classification cases. Classification 1 targeting the volume coefficient with the classes $c_{v,1} = 0.2$ and $c_{v,2} = 0.35$ and classification 2 the inclusion diameter with the classes $d_{inc,1} = 0.05$ mm and $d_{inc,2} = 0.1$ mm.

B. CLASSIFICATION OF SPECIFIC MATERIAL PROPERTIES

In this section we will show that the acquisition of the HYP tissues' specific microstructure is possible using the targeted evaluation of the power reflection coefficient used as a spectral fingerprint by ANNs within specific frequency intervals.

For this purpose, we will perform a binary classification with respect to the volume fraction c_v and the cell diameter d_{inc}. To implement the binary classification, the output layer of the ANNs used is reduced to two neurons (cf. Fig. 11(a)). In addition to the modification of the ANN's output layer, we will reorganize the spectral fingerprints of the parameter sets $\tilde{P}_1$ to $\tilde{P}_4$ according to Fig. 11(b). The material parameter indicating the classification target is now considered as the primary parameter and the other as the secondary one acting as a perturbation. Following this principle, parameter sets of the same primary parameters are grouped together into two classes of the same size. As a result, we obtain two classification cases which still include all of the 800 realizations.

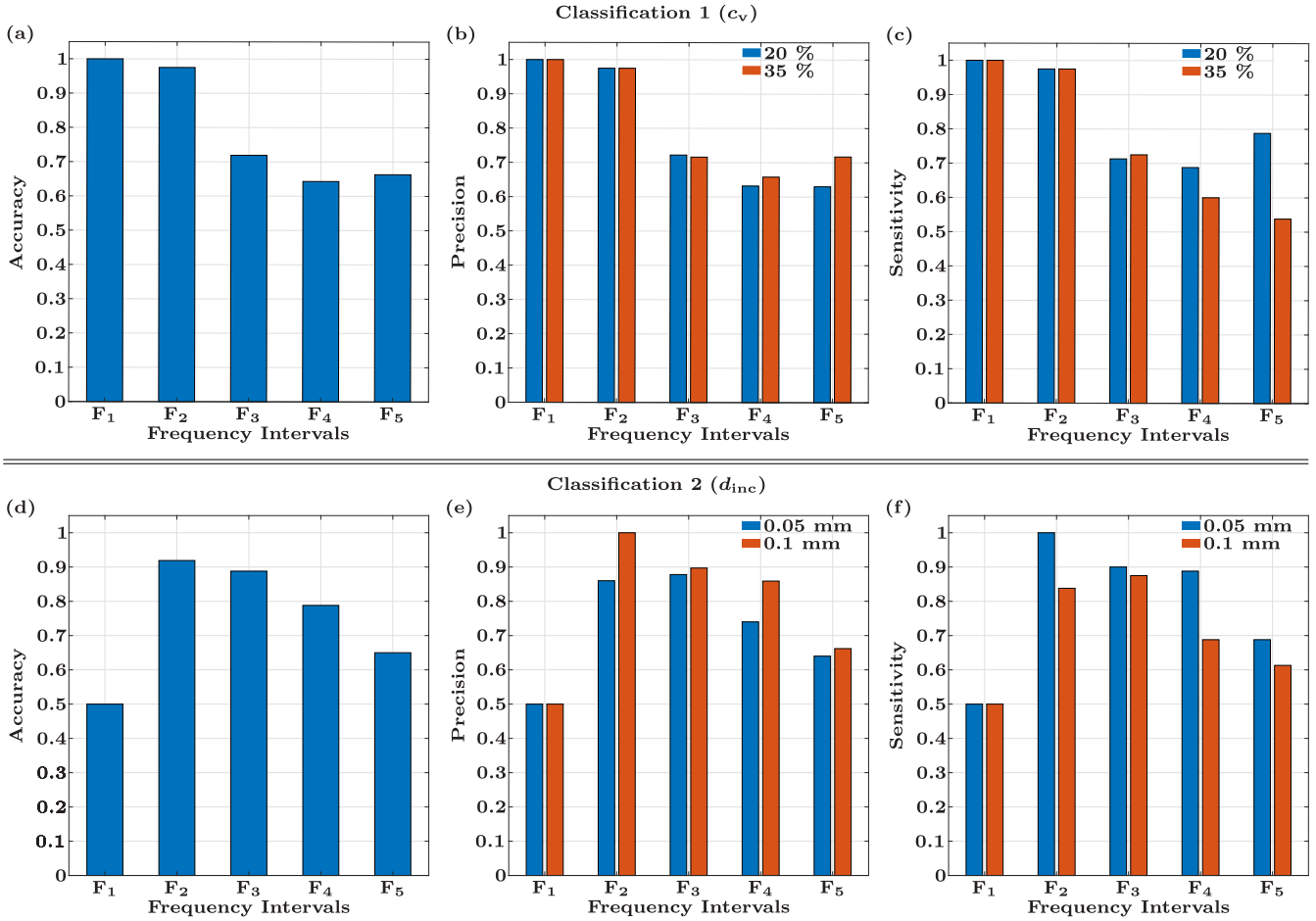

FIGURE 12. Results of the material classification based on the implemented binary classification scheme: The top row, (a) to (c), shows the classification results of the neural networks which had the aim of identifying the volume fraction and the bottom row, (d) to (f), shows the classification results with the aim of identifying the inclusion diameter. The diagrams on the left-hand side show the accuracy of the characterizations, those in the middle the precision and those on the right-hand side the sensitivity of the classifications within the frequency ranges F_1 to F_5.

To investigate the frequency specificity of the classification, the analyzed spectral range is rearranged and subdivided into 5 new frequency intervals F_1 to F_5. The interval $F_1 :=$ [10 MHz; 10 GHz] covers the validity range up to a point where no significant variance in the reflection coefficient of the heterogeneous model exists. $F_2 :=$ [10 GHz; 100 GHz] includes an extended transition range between the validity and forbidden range including the validity limit. In contrast, $F_3 :=$ [100 GHz; 150 GHz], $F_4 :=$ [150 GHz; 175 GHz], and $F_5 :=$ [175 GHz; 200 GHz] are all consecutive sub-intervals in the forbidden frequency range (c.f. Fig. 8).

The results of the HYP tissue classifications are quantified using the metrics introduced above and are illustrated in Fig. 12. The upper row (a)-(c) shows the results of classification 1 for the identification of the volume fraction c_v within all frequency intervals F_1 to F_5, whereas the lower row (d)-(f) displays the corresponding results of classification 2 for the cell diameter d_{inc}. The accuracy, precision and sensitivity of the prediction within classification 1 confirms (as conjectured) that the frequency intervals F_1 and F_2 are best suited to predict aggregate quantities of the microstructure such as the volume fraction c_v (with measures better than 98 %). This predominantly corresponds to the allowed frequency band below the validity limit. In contrast, the prediction quality drops considerably (and becomes imbalanced between classified volume fractions) for the residual higher frequency intervals in the forbidden frequency range. This conclusion is also supported by the analysis of classification 2, which aims to identify the cell diameter d_{inc}. Given the particular parameter sets, the frequency intervals F_2 - F_4 or F_3 and F_4 within the forbidden frequency range were found to be well-suited to the prediction of the microscopic quantities of the underlying microstructure. The strong predictive power of frequency interval F_2 leads to the conjecture that the transition region around the validity limit encompassing both allowed and forbidden frequency ranges could be particularly fertile with respect to potential information on the underlying microstructure. For this reason, the next section addresses how to identify frequency domains that are relevant for the classification of specific microscopic properties.

C. OPTIMIZATION OF THE CLASSIFICATION BASED ON OCCLUSION SENSITIVITY

The emerging question is how to separate frequency intervals which bear specific information about the tissue's microstructure from those which do not. To answer this question, we have developed a method based on occlusion sensitivity [27], which we will call the occlusion sensitivity method (OSM) in the following. The basic idea is to cover parts of an image with a mask (having an extent that corresponds to a certain frequency range) and quantify its influence on object recognition. The method developed is explained using the data for the classification of the inclusion diameter in interval F_2 as an example.

A detailed overview of how the OSM is implemented and modified in order to separate frequency intervals which are important from those which are not is illustrated in Fig. 13(a). In a first step, the spectral fingerprint of a single microstructure (still represented by an 1D grayscale image) is reproduced in its entirety as many times as the number of pixels it contains, in this case 300. Then, these copies are grouped into a batch and modified by a mask of arbitrary odd pixel length placed in a position shifted by one pixel in each subsequent copy. To enable the mask to hide the information content of the covered pixels without having an over-weighted influence on the pattern recognition of the ANN, the gray value of the mask corresponds to the average value of the grayscale image under consideration.

Finally, the masked batch is transferred to the ANN trained in Sec. V-B to predict the inclusion diameter between 10 and 100 GHz (F_2) and the influence of this masking process on the classification is determined. This is done by observing the change in the classification result calculated by the output layer of the ANN, i.e. the softmax function. In the case of our binary classification, the output of the softmax function, the precision score, is a number between 0 and 1 which expresses the probability of belonging to a certain class. A prediction score > 0.5 (shaded in blue) means that the ANN has interpreted the spectral response as originating from a microstructure with an inclusion diameter of $d_{\mathrm{inc},1} = 0.05$ mm and a prediction score < 0.5 (shaded in red) as originating from a material structure with an inclusion diameter of $d_{\mathrm{inc},2} = 0.1$ mm. An example of how this procedure is actually implemented is given in Fig. 13(b) and (c), using the spectral response of a realization with a volume coefficient of $c_{\mathrm{v}} = 0.2$ and an inclusion diameter of $d_{\mathrm{inc}} = 0.1$ mm. The coded 1D grayscale image of this particular realization is located above the corresponding curve of the reflection coefficient and represents the input data within the schematic shown in Fig. 13(a). The dotted blue and dashed red curves correspond to reproductions of the original spectral response, where the masks are centered on the frequency points f_{m} and f_{n} (cf. masked batch in Fig. 13(a)). The curve of the prediction score in Fig. 13(c) can be determined by the sequential classification of all masked reproductions by the ANN (cf. prediction score in Fig. 13(a)). In analogy to the grayscale coding of the spectral fingerprint, the

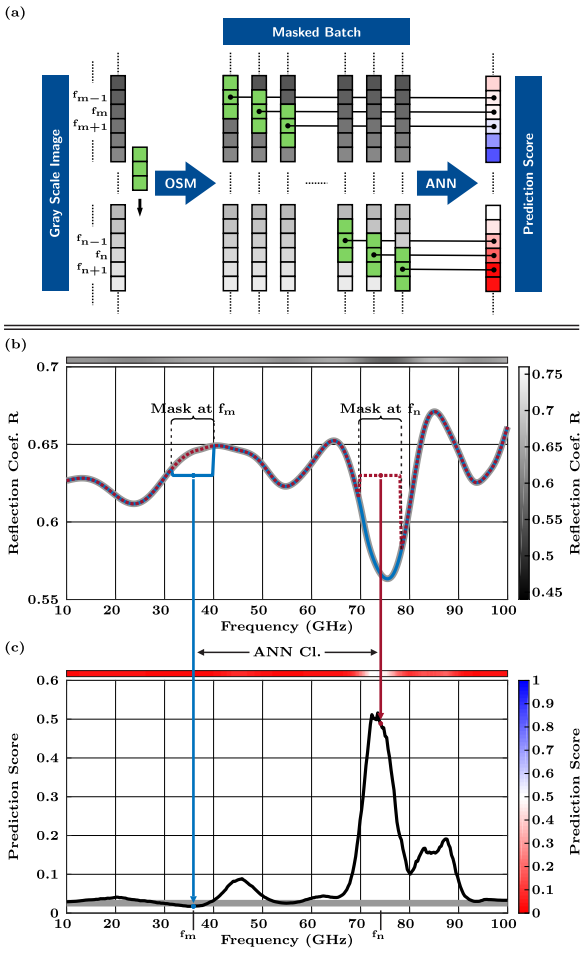

FIGURE 13. Basic idea of the OSM developed here: (a) Schematic of the proposed procedure for the separation of information-carrying frequency ranges for the optimization of the frequency specific classification of specific features of the tissue's microstructure. (b) The reflection coefficient of one realization with a volume coefficient $c_{\mathrm{v}} = 0.2$ and inclusion diameter $d_{\mathrm{inc}} = 0.1$ mm between 10 to 100 GHz. The gray bar above displays the reflection coefficient of this particular realization. The color bar associated with this code is located to the right of the graph. The blue dotted and red dashed lines show reproductions of the original reflection coefficient modified by masks. The center of the mask is centrally aligned with the sampled frequency points f_{n} and f_{m}, respectively. (c) depicts the precision score of the modified reproductions (such as the blue dotted and red dashed curve). The prediction score at each frequency point is associated with the center position of the corresponding mask. The gray constant represents the prediction score of the realization's original reflection coefficient. The red bar above the graph displays the prediction score in accordance with the color bar to the right of the diagram.

prediction score is also color-coded and displayed as a red shaded bar placed above the graph. The prediction score at each frequency point is associated with the center position of the corresponding mask, illustrated by the arrows connecting Fig. 13(b) and (c). To assess the influence of the mask relative to the prediction score of the original (unmasked) fingerprint, it is also plotted as a gray-shaded constant.

If this procedure is not applied to a single implementation but to the spectral response of all 160 classified realizations of the test set between 10 GHz and 100 GHz, a 2D grayscale image is obtained as shown in Fig. 14(a). In this

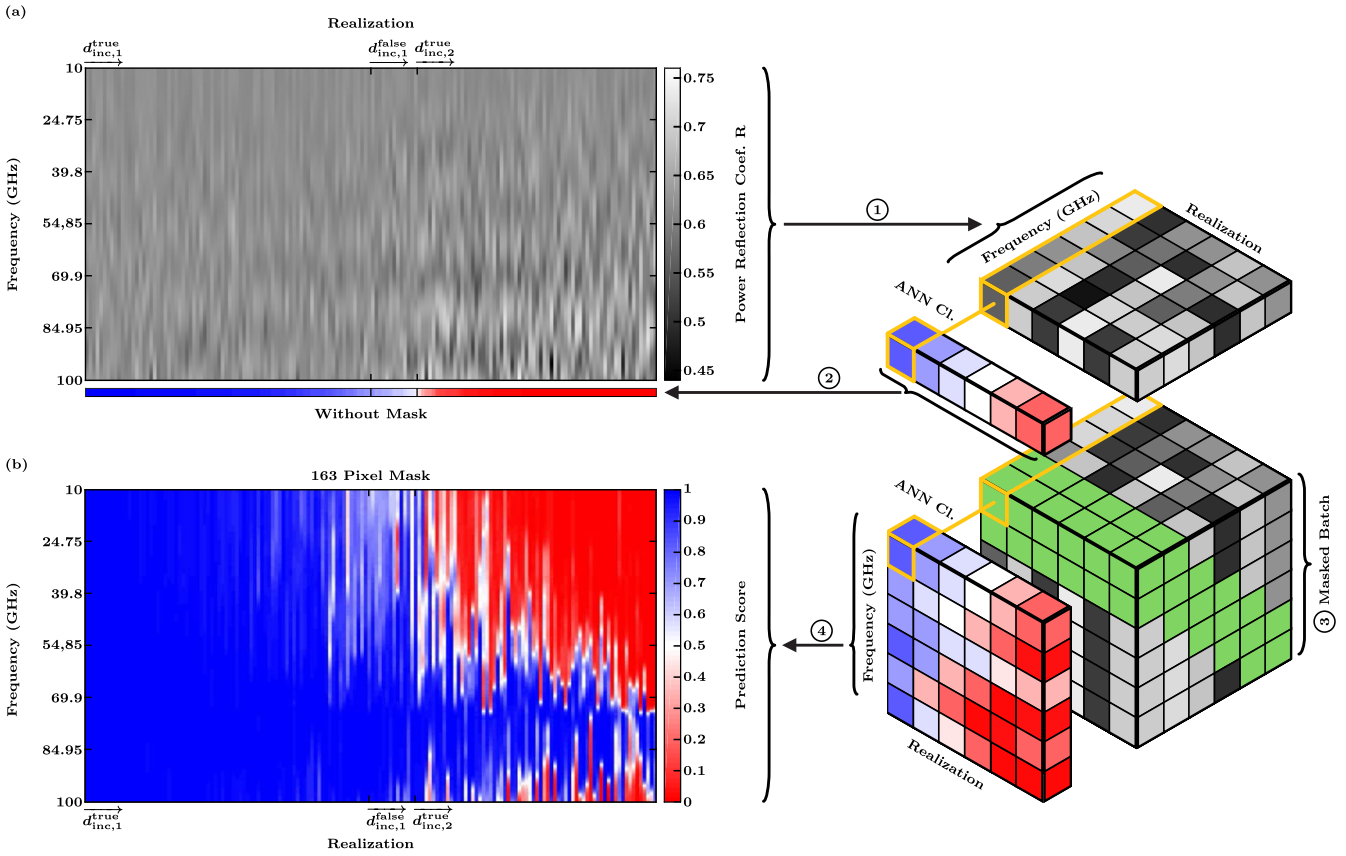

FIGURE 14. Application of the OSM to 160 realizations (test set): (a) Grayscale image of 160 realizations. Every pixel in the horizontal direction represents one realization and every pixel in the vertical direction the power reflection coefficient R at a sampled frequency point in the frequency range between 10 GHz to 100 GHz. These spectral responses are ordered from left to right according to its prediction score. $d^{\text{true}}_{\text{inc},1}$ marks realizations correctly assigned to the class $d_{\text{inc},1} = 0.05$ mm, $d^{\text{false}}_{\text{inc},1}$ marks those incorrectly assigned to $d_{\text{inc},1} = 0.05$ mm and $d^{\text{true}}_{\text{inc},2}$ marks those correctly assigned to $d_{\text{inc},2} = 0.1$ mm. (b) Blue-red image of the prediction score generated by applying the OSM-based optimization procedure to all 160 realizations for a mask size of 163 pixel. The deviation of the prediction score of the original (unmasked) fingerprints with the prediction score of their masked reproductions at a specific frequency point indicates the importance of the frequency patterns covered by these masks.

grayscale image, every pixel in the horizontal direction represents one realization and every pixel in the vertical direction the power reflection coefficient, R, at a certain frequency (between 10 GHz to 100 GHz). The shade varies from black for the lowest R in this frequency range (approximately 0.45) to white for the highest R (approximately 0.75). To help relate the data to the procedure presented in Fig. 13, this grayscale image is illustrated in the adjacent figure in simplified form as a pixel map ①. After classification, the spectral response of each realization is ordered from left to right according to its prediction score, displayed as a narrow bar below the grayscale image ②. The color bar associated with the prediction score is placed next to Fig. 14(b). Realizations with an inclusion diameter of $d_{\text{inc},1} = 0.05$ mm which have been correctly identified are labeled as $d^{\text{true}}_{\text{inc},1}$ and those with an inclusion diameter of $d_{\text{inc},2} = 0.1$ mm are labeled as $d^{\text{true}}_{\text{inc},2}$ or $d^{\text{false}}_{\text{inc},1}$ respectively, if the classification is correct or incorrect. The reordered grayscale image is reproduced (vertically) to form a cube in illustration ③. The reproductions of the spectral fingerprints in this cube are also modified by masks indicated by green voxels. Each of the modified realizations of the batch is then classified by the ANN. The result of this classification is a 2D red-blue image that documents the influence of the masking for each of the considered realizations against the frequency ④. With this procedure applied to the realizations shown in Fig. 14(a) with a mask size of 163 pixels, Fig. 14(b) is obtained. By relating the prediction score of the unmasked spectral fingerprints to Fig. 14(b), the deviation between them can be interpreted as the sensitivity of the ANN to the masked interference patterns (not in terms of the metrics introduced earlier), so that the importance of these patterns can be assessed. Assessing Fig. 14(b) in this way, we can conclude from the strong misclassification of previously correctly identified realizations with an inclusion diameter of $d_{\text{inc},2} = 0.1$ mm ($d^{\text{true}}_{\text{inc},2}$) that the frequency response between 40 and 100 GHz plays a major role in the correct classification of the material structure by the ANN. Therefore, new frequency intervals for optimized classification are defined: $\tilde{\text{F}}_1 := [10\text{ GHz}; 40\text{ GHz}]$, $\tilde{\text{F}}_2 := [40\text{ GHz}; 100\text{ GHz}]$ and $\tilde{\text{F}}_3 := [40\text{ GHz}; 110\text{ GHz}]$.

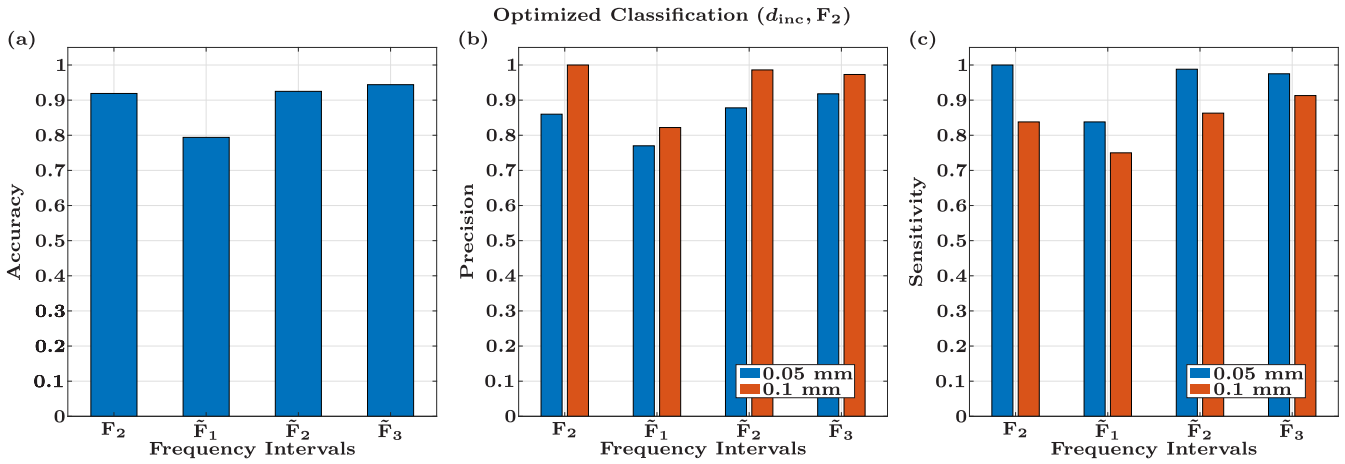

FIGURE 15. Classification results with the aim of identifying the inclusion diameter in the original frequency interval $\mathrm{F_2}$ and in the modified intervals $\tilde{\mathrm{F}}_1$ to $\tilde{\mathrm{F}}_3$. The diagram on the left-hand side shows the accuracy of the characterizations, the one in the middle the precision and the one on the right-hand side, the sensitivity of the classifications.

The results of this optimized classification are depicted in Fig. 15. Comparing the original frequency interval $\mathrm{F_2}$ (from Fig. 12) with the frequency interval $\tilde{\mathrm{F}}_1$, it can be seen that the accuracy decreases from 91.9 % to 79.4 %. This indicates that the information contained in interval $\tilde{\mathrm{F}}_1$ has decreased. By comparing $\mathrm{F_2}$ with $\tilde{\mathrm{F}}_2$ on the other hand, it can be seen that the prediction accuracy has increased slightly from 91.9 % to 92.5 % and in addition, the asymmetry in precision and sensitivity has decreased. If $\tilde{\mathrm{F}}_2$ is extended by 10 GHz to 110 GHz in $\tilde{\mathrm{F}}_3$, the accuracy can be increased by 1.9 % percent and the asymmetry decreases further.

Based on these results it can be shown that the reflection coefficient contains enough information about specific features of the tissue's microstructure in specific frequency intervals to be used as a spectral fingerprint. Furthermore, based on the OSM, we were able to develop a procedure that selects and visualizes these information-bearing frequency intervals.

VI. SUMMARY AND CONCLUSION

In this study, we presented a three-stage methodology in the framework of a parametrizable multiscale EM simulation workbench yielding the effective EM material properties of a (bio-)composite. This methodology considers both anisotropy and dispersion, which are rooted in the precise cellular structure of the composite. In a subsequent step these homogenized material models were evaluated in terms of their validity limit. This limit was determined as the frequency at which a deviation of 2 % occurred between the frequency responses of the heterogeneous (bio-)composite (reference model) and its homogeneous representation in a generic reflectometry setup. In this setup, both materials were illuminated by an EM plane wave. In our study we focused on a 2D analysis of generic but suitable HYP representations of a complex tissue composite. Since the validity of homogenization at the tissue level is the main focus of the intended multi-scale modeling approach, the HYP representations investigated were modeled as randomized cell arrangements.

The modeling and simulation of a large number of realizations of these HYP structures in Sec. III led to a comprehensive Monte-Carlo analysis of various generic HYP derivatives. As part of this analysis we developed a statistical measure to determine the validity limit of the implemented quasi-static homogenization approach. This allows us to divide the spectral response of the reflection into a validity range in which the homogenization is valid, and a forbidden range in which it is not. The results of this analysis revealed that the applicability of the homogeneous material representation had an upper operating frequency limit that started at surprisingly low frequencies in the low mm-wave range and thus contradicted the traditional use of homogenized layer models in tissue analysis/diagnostics [12], [17]. This forced any hierarchically organized multiscale model topology to become strongly tied to a corresponding operating frequency bandwidth. Consequently, an ultra-wideband tissue analysis must consider simultaneous structural changes in the tissue models during frequency domain simulation by using different models to represent different frequency ranges.

Sec. IV showed that the collapse of the EMT approximation coincided with an increasing impact of the tissue's underlying microstructure on the frequency response beyond the validity limit. In the course of this study, the difference between the electric and magnetic energy densities displayed particularly strong resonances and standing fields which correlated highly with the tissue microstructure and thus with the randomized HYP cell distribution. Explaining the relationship between the resonances in the underlying microstructure and interference patterns in the spectral response of the reflection coefficient, we were able to establish reflection as a spectral fingerprint to classify features of the tissue's microstructure. Following this idea, we extended the Monte-Carlo analysis by including parameter sets with

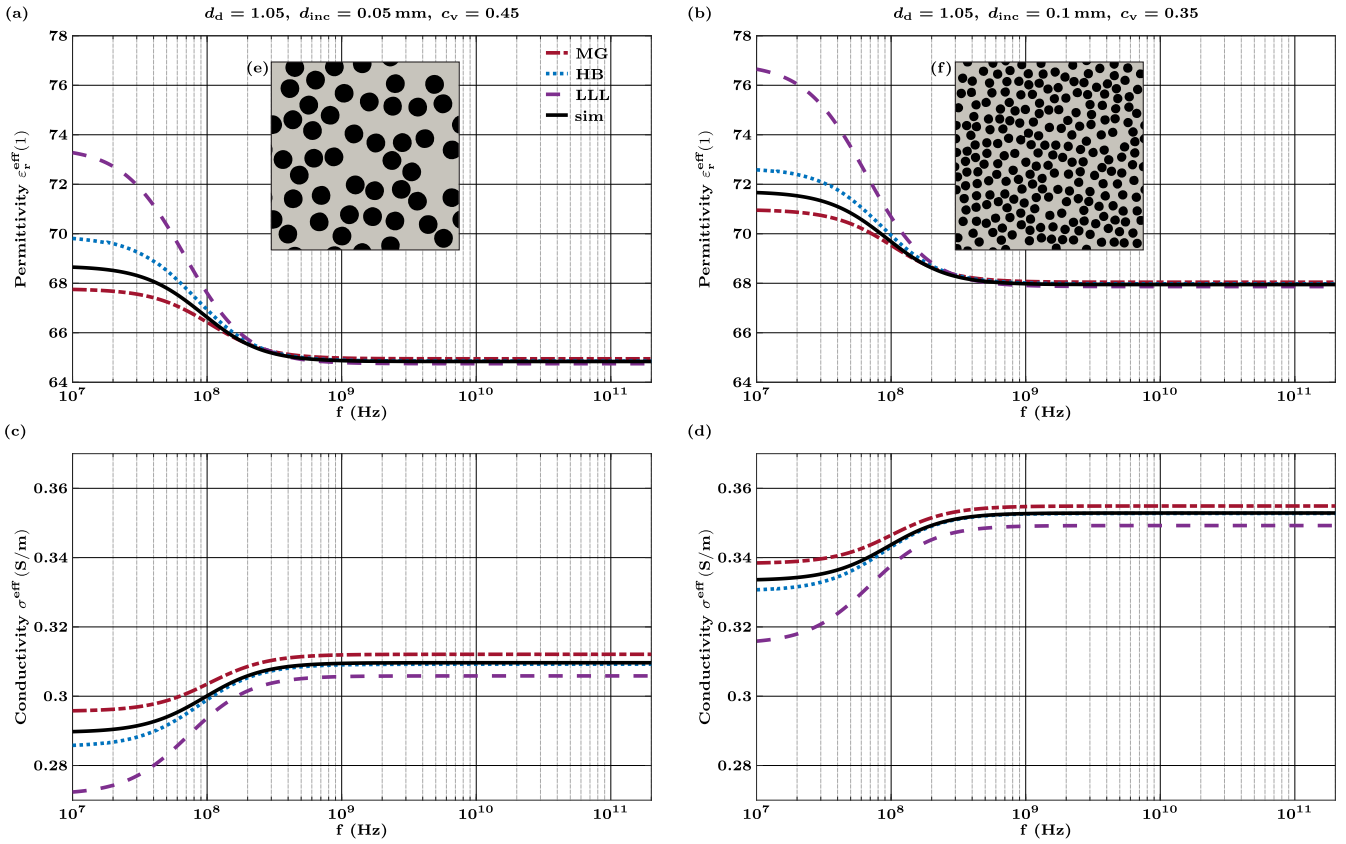

FIGURE 16. Spectral response of the permittivity and conductivity of two illustrative microstructures in the frequency range from 10 MHz to 200 GHz. The spectra are calculated by analytical mixing rules such as Maxwell-Garnett (MG), Hanai-Bruggemann (HB) and Landau-Lifshitz-Looyenga (LLL) as well as by using numerical simulations. Fig. (a) and (c) correspond to the structural parameters $d_d = 1.05$, $d_{inc} = 0.05$, $c_v = 0.45$ and Fig. (b) and (d) to $d_d = 1.05$, $d_{inc} = 0.1$, $c_v = 0.35$. Examples for the analyzed HYP realizations are shown in (e) and (f).

variable structural parameters for the inclusion diameter and the volume fraction of the lipid droplets, and identified the resulting HYP derivatives with an image recognition-based material classification procedure using ANN in Sec. V. Based on this classification we showed that the valid and the forbidden frequency ranges complemented each other with regard to the information content of the spectral fingerprint. In addition, we were able to show that the forbidden frequency range could be exploited to predict the microstructures of the HYP tissues (e.g. the expectation values of the cell sizes) and the validity range to classify aggregated HYP tissue properties such as the volume fractions of the adipose cells. In Sec. V-C, we developed a method based on occlusion sensitivity to identify and subsequently select information-carrying frequency rangeswhich can be correlated to specific structural properties of the microstructure.

OUTLOOK

On the basis of these research results, the following priorities emerge for the future. Validity limits caused by structural/morphological signatures in the frequency response of reflection in the forbidden range will be further researched and documented. For this purpose, specially designed 2D composites will be created using 3D printing and used to make measurements for comparison with corresponding simulations. This will explore the EM signatures in the forbidden range for composites with low material contrast. In addition, structures with embedded channels filled with liquids (e.g. water, alcohol) will be examined to investigate the separation of signatures originating in the morphology/structure and those in the dispersive EM properties of the constituents of the composite. A further future focus will be the expansion of the virtual workbench for the exploration of multi-layer structures. The central question is how much the underlying microstructure of the individual layers of the tissue can be superimposed in the frequency response and still be separated regarding the allowed operating frequency bands of the EMT models of these layers as expressed by their validity limits. The aim will be to identify and analyze subfrequency bands in order to extract information from individual layers and to deduce a complete image of the material system using ANNs in a wideband analysis. Furthermore, the question arises to what extent the roughness of the material surface has an influence on the analysis of a composite. This question can be divided into two parts: firstly, whether volume and surface scattering can be separated and secondly, whether the type of discretization has an influence on the result when simulating reflection events at a rough material boundary layer.

APPENDIX A
ADDITIONAL NOTES REGARDING HOMOGENIZATION

An alternative or rather an approximation to the numerical homogenization procedure presented in Sec. II-B is the application of classical mixing rules provided by EMT [24]. However, the reasons in favor of the implemented numerical homogenization procedure are not self-explanatory. This is why the differences to common mixing rules will be discussed in the following.

Classical mixing rules such as Maxwell-Garnett (MG), Bruggemann (B) [28] or Landau-Lifshitz-Looyenga (LLL) [29], [30] consider two-phase composites as inclusions embedded in a dielectric host material. The derivation of classical mixing rules, which analytically describe the macroscopic material properties of such a material mixture, is based on the following assumptions: the EM field solution is curl-free ($\nabla \times \underline{\vec{E}} = 0$) and all interactions between adjacent inclusions are neglected [31]. Strictly speaking, these assumptions mean that the application of the mixing rules is limited to quasi-static conditions in diluted mixtures. As a rule of thumb, the relation $\frac{\lambda_m}{2\pi} > d_{inc}$, where λ_m denotes the wavelength within the material, can be used to estimate the upper applicable frequency of the mixing rules of sparse microstructures (c_v up to 10 %).

In [32], Bruggeman's mixing rule was extended to the Hanai-Bruggeman (HB) formula to approximate denser mixtures (c_v up to 40 % [33]). The macroscopic material properties according to HB can be determined by:

$$0 = \frac{(\varepsilon_{r,BG}^{eff} - \varepsilon_{r,2}^{eff})}{(\varepsilon_{r,1}^{eff} - \varepsilon_{r,2}^{eff})} \cdot \left(\frac{\varepsilon_{r,2}^{eff}}{\varepsilon_{r,BG}^{eff}} \right)^{A} - (1 - c_v) \tag{8}$$

where $\varepsilon_{r,1}^{eff}$ and $\varepsilon_{r,2}^{eff}$ denote the effective complex permittivity of the host and inclusion material respectively. The depolarization factor $A = 0.5$ accounts for composites consisting of rods embedded in a dielectric host material. According to MG, the effective material parameters can be determined by

$$\varepsilon_{r,MG}^{eff} = \varepsilon_{r,1}^{eff} \cdot \frac{(\varepsilon_{r,1}^{eff}(1 - c_v)(1 - A) + \varepsilon_{r,2}^{eff}(c_v + A(1 - c_v)))}{\varepsilon_{r,2}^{eff} + A(1 - c_v)(\varepsilon_{r,2}^{eff} - \varepsilon_{r,1}^{eff})} \tag{9}$$

and according to LLL by

$$\varepsilon_{r,LLL}^{eff} = \varepsilon_{r,1}^{eff\ (1-c_v)} \cdot \varepsilon_{r,2}^{eff\ c_v}. \tag{10}$$

In Fig. 16, the spectra of the permittivity and conductivity calculated by MG, HB and LLL mixing rules are compared with those determined by numerical simulations. Fig. 16 (a) and (c) show the permittivity and conductivity of a microstructure with the parameter set $d_d = 1.05$, $d_{inc} = 0.05$ and $c_v = 0.45$ and Fig. (b) and (d) one with the parameter set $d_d = 1.05$, $d_{inc} = 0.1$ and $c_v = 0.35$. Examples of the analyzed HYP realizations are shown in (e) and (f). These cases represent extremes in terms of the volume fraction or density applied to the mixing rules.

Common to all spectra is a low-frequency roll-off of permittivity, or a increase of conductivity, at about 100 MHz,

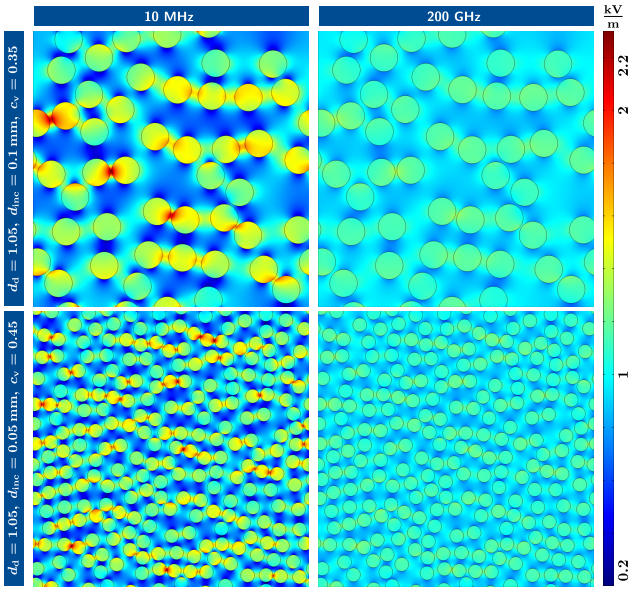

FIGURE 17. Graphical evaluation of the electric field within the microstructures under investigation at 10 MHz and 200 GHz (i.e. with and without the influence of charge carriers between the material boundaries). The images all demonstrate rotation-free yet divergent electric fields.

which is associated to the decay of the Maxwell-Wagner effect. In the lower frequency range, the simulated spectra are between those of MG and HB. The calculations according to the MG formula represent a lower estimate and the HB an upper estimate of the EM material properties. The calculations according to the LLL formula seem to overestimate the influence of interfacial polarization and, thus, are not appropriate to represent the macroscopic material properties in the lower frequency range. At high frequencies, however, the deviation between the simulation results and any of the mixing rules is marginal.

This result is in accordance with [22], where the dielectric spectra obtained by simulations and mixing rules have been compared. The investigations showed that only numerical simulations which can be considered as the multipole representation of the EM problem are able to determine the influence of interactions between adjacent particles correctly at low frequencies. In [15] and more comprehensively in [20] numerical homogenization has been extensively investigated and validated using skin measurements, in the context of multi-scale modeling of the skin at microwave frequencies in comparison with classical mixing rules. It has been shown that the shape of cells has a significant influence on the macroscopic material properties due to interfacial polarization, especially at low frequencies and high volume densities.

The effect of interfacial polarization is illustrated in Fig. 17 by means of the electric field strength distribution at 10 MHz and 200 GHz within the illustrative microstructures considered in Fig. 16. Even though the numerical FEM solver uses all of Maxwell's equations, the excitation of the composite by two electrodes means that the images all demonstrate rotation-free yet divergent electric fields. Compared to classical mixing rules at frequencies lower than

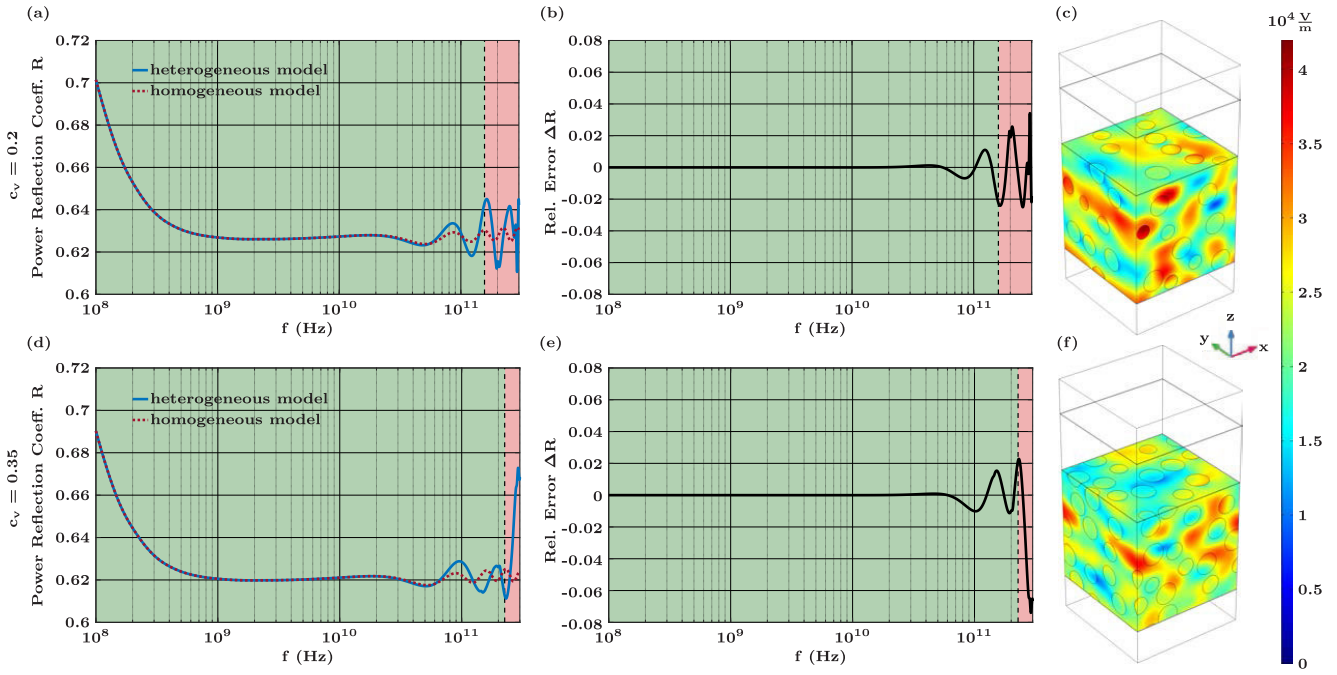

FIGURE 18. Overview of two 3D simulations of a generic HYP structure (i.e. for $\varepsilon_{r,1} = 80$; $\sigma_1 = 0.53$ S/m; $\varepsilon_{r,2} = 50$; $\sigma_2 = 0.12$ S/m; $d_{inc} = 50$ μm). The edge length of the simulated supercell is 0.25 mm. The upper row contains simulation results for a structure with a volume fraction of $c_v = 0.2$ and the bottom row those of a structure with a volume fraction of $c_v = 0.35$. (a) and (d) show the frequency-dependent power reflection coefficient R of the heterogeneous (blue) and the homogeneous model (red). (b) and (e) provide an overview of the relative error between both models. The validity range is highlighted in green and the forbidden frequency range in red. (c) and (f) show the field distribution of the magnitude of the electric field within the supercell embedded in the simulation setup at 300 GHz.

the roll-off frequency of the interfacial polarization, numerical homogenization can therefore still be regarded as the more reliable calculation method, which considers field interactions between adjacent inclusions, but still provides a quasi-static solution.

Nevertheless, MG and HB mixing rules can be used to estimate the validity at low frequencies and can calculate the macroscopic material properties with high accuracy for high frequencies even for dense composites when compared to numerical simulations.

In summary, at frequencies lower than the expected Maxwell-Wagner roll-off, while MG and HB can be considered as upper and lower bounds to verify numerical simulation, LLL overestimates the interfacial polarization. At frequencies lower than the expected Maxwell-Wagner roll-off, the differences between the spectra obtained by simulations or determined by mixing rules are negligible, so that the calculation methods are interchangeable. Therefore, classical mixing rules can be used instead of the numerical EMT model to estimate the validity limits as proposed in Sec. III.

APPENDIX B
3D REFERENCE SIMULATION

The transferability of the research results is checked by simulating two three-dimensional microstructures, one with a volume coefficient of $c_v = 0.2$ and the other with $c_v = 0.35$. As shown in Fig. 18(c) and (f), microstructures with spherical inclusions embedded in a cubic supercell are investigated. While the material parameters and the diameter of the inclusion, $d_{inc} = 0.05$ mm, remain unchanged to those introduced in Sec. II, the edge length of the cubic supercell is now reduced to 0.25 mm. To reduce the numerical demands of the simulation, an auxiliary layer has been inserted between the supercell and the PML. Just like the bottom PML, the effective material parameters of the composite are assigned to this auxiliary layer. Note that this separation of the supercell by this auxiliary layer is mainly due to numerical reasons as the direct termination of the heterogeneous layer by the PML poses some numerical challenges given the layer's complex morphology.

Due to the high numerical demand and, thus, to the high simulation time, this investigation could not be performed with a larger set of implementations. The simulations have been performed on a PC equipped with two Intel Xeon E5-2697 V4 processors (36 cores) and 512 GB of RAM. Between 0.1 GHz and 300 GHz, 200 frequency points have been simulated with a MUMPS solver with the density of these points increasing with frequency. The simulation for each frequency point lasts 2 hours and includes the full-wave simulation of the heterogeneous microstructure and its homogenized representative in p and s-polarization.

The spectral response of the power reflection coefficient R is shown for the heterogeneous (blue) and homogeneous model (red) in the given frequency interval in Fig. 18(a) and (d). Based on the 2 % deviation criterion, the validity of the homogeneous material model is retrieved from the

relative deviation (i.e. relative error) between the models and collapses at 156 GHz for the material structure with a volume coefficient of $c_v = 0.2$ and at 225 GHz for $c_v = 0.35$. The validity range of the homogeneous model is again marked green and the forbidden range red.

The observed periodic oscillations in the simulated spectral response of the power reflection are due to Fabry-Perot resonances in both the heterogeneous and homogeneous layer. These oscillations are determined by the finite thickness of the auxiliary layers and are thus not present in our prior 2D simulations. This is because we have dealt with a numerically infinite half-space system in those cases. However, the evaluation of the validity limit is not affected by the Fabry-Perot resonances since they are present in both models and thus assumed to be balanced out in the analysis of the relative error. To underline this, Fig. 18(b) and (e) show the relative errors between the reflection coefficients of both models in the same frequency range.

The field strength distributions within the heterogeneous models at 300 GHz illustrated in Fig. 18(c) and (f) show that the breakdown of the validity of the EMT model and the associated interference patterns in the reflection response are accompanied by strong field inhomogeneities within the microstructure. Both the separation of the investigated spectrum into a valid and a forbidden range, and the interference patterns associated with inhomogeneous field distributions in the microstructure in the forbidden range clearly indicate the transferability of one of the paper's core statements to randomized three-dimensional microstructures. This statement concerned the correlation of interference patterns in the spectral response with morphological peculiarities of the microstructure. However, the transferability of the paper's quantitative statements is not given here.

ACKNOWLEDGMENT

The authors would like to thank the technical support of V. Gerhardt, K. Maess, and B. Morley, as well as scientific contributions from K. Ehlen, J. Maibaum, and J. Assmann.

REFERENCES

[1] P. Hillger, M. van Delden, U. S. M. Thanthrige, A. M. Ahmed, J. Wittemeier, K. Arzi, M. Andree, B. Sievert, W. Prost, A. Rennings, D. Erni, T. Musch, N. Weimann, A. Sezgin, N. Pohl, and U. R. Pfeiffer, "Toward mobile integrated electronic systems at THz frequencies," *J. Infr., Millim., THz Waves*, vol. 41, no. 7, pp. 846–869, Jul. 2020.

[2] J. Barowski, M. Zimmermanns, and I. Rolfes, "Millimeter-wave characterization of dielectric materials using calibrated FMCW transceivers," *IEEE Trans. Microw. Theory Techn.*, vol. 66, no. 8, pp. 3683–3689, Aug. 2018.

[3] J. Barowski, J. Jebramcik, I. Alawneh, F. Sheikh, T. Kaiser, and I. Rolfes, "A compact measurement setup for *in-situ* material characterization in the lower THz range," in *Proc. 2nd Int. Workshop Mobile THz Syst. (IWMTS)*, Bad Neuenahr, Germany, Jul. 2019, pp. 1–5.

[4] J. Dong, B. Kim, A. Locquet, P. McKeon, N. Declercq, and D. S. Citrin, "Nondestructive evaluation of forced delamination in glass fiber-reinforced composites by terahertz and ultrasonic waves," *Compos. B, Eng.*, vol. 79, pp. 667–675, Sep. 2015.

[5] J. Dong, A. Locquet, N. F. Declercq, and D. S. Citrin, "Polarization-resolved terahertz imaging of intra- and inter-laminar damages in hybrid fiber-reinforced composite laminate subject to low-velocity impact," *Compos. B, Eng.*, vol. 92, pp. 167–174, May 2016.

[6] L. Afsah-Hejri, P. Hajeb, P. Ara, and R. J. Ehsani, "A comprehensive review on food applications of terahertz spectroscopy and imaging," *Comprehensive Rev. Food Sci. Food Saf.*, vol. 18, no. 5, pp. 1563–1621, Sep. 2019.

[7] X. Hu, W. Lang, W. Liu, X. Xu, J. Yang, and L. Zheng, "A non-destructive terahertz spectroscopy-based method for transgenic rice seed discrimination via sparse representation," *J. Infr., Millim., THz Waves*, vol. 38, no. 8, pp. 980–991, Aug. 2017.

[8] F. Topfer and J. Oberhammer, "Millimeter-wave tissue diagnosis: The most promising fields for medical applications," *IEEE Microw. Mag.*, vol. 16, no. 4, pp. 97–113, May 2015.

[9] D. Oppelt, J. Adametz, J. Groh, O. Goertz, and M. Vossiek, "MIMO-SAR based millimeter-wave imaging for contactless assessment of burned skin," in *IEEE MTT-S Int. Microw. Symp. Dig.*, Honolulu, HI, USA, Jun. 2017, pp. 1383–1386.

[10] X. Yang, X. Zhao, K. Yang, Y. Liu, Y. Liu, W. Fu, and Y. Luo, "Biomedical applications of terahertz spectroscopy and imaging," *Trends Biotechnol.*, vol. 34, no. 10, pp. 810–824, Oct. 2016.

[11] K. I. Zaytsev, I. N. Dolganova, N. V. Chernomyrdin, G. M. Katyba, A. A. Gavdush, O. P. Cherkasova, G. Komandin, M. A. Shchedrina, A. N. Khodan, D. S. Ponomarev, I. V. Reshetov, V. Karasik, M. Skorobogatiy, V. N. Kurlov, and V. V. Tuchin, "The progress and perspectives of terahertz technology for diagnosis of neoplasms: A review," *J. Opt.*, vol. 22, no. 1, pp. 1–44, 2019.

[12] S. I. Alekseev and M. C. Ziskin, "Human skin permittivity determined by millimeter wave reflection measurements," *Bioelectromagnetics*, vol. 28, no. 5, pp. 331–339, 2007.

[13] G. Piro, P. Bia, G. Boggia, D. Caratelli, L. A. Grieco, and L. Mescia, "Terahertz electromagnetic field propagation in human tissues: A study on communication capabilities," *Nano Commun. Netw.*, vol. 10, pp. 51–59, Dec. 2016.

[14] S. Huclova, D. Erni, and J. Froehlich, "Modelling effective dielectric properties of materials containing diverse types of biological cells," *J. Phys. D, Appl. Phys.*, vol. 43, no. 36, pp. 365405-1–365405-10, Sep. 2010.

[15] S. Huclova, D. Erni, and J. Fröhlich, "Modelling and validation of dielectric properties of human skin in the MHz region focusing on skin layer morphology and material composition," *J. Phys. D, Appl. Phys.*, vol. 45, no. 2, pp. 025301-1–025301-17, Jan. 2012.

[16] J. Froelich, S. Huclova, and D. Erni, "Accurate multi-scale skin model suitable for determining sensitivity specificity changes skin components," in *Computational Biophysics of the Skin*, B. Querleux, Ed. Singapore: Pan Stanford Publishing, 2014, ch. 12, pp. 353–394.

[17] M. Saviz, L. M. Toko, O. Spathmann, J. Streckert, V. Hansen, M. Clemens, and R. Faraji-Dana, "A new open-source toolbox for estimating the electrical properties of biological tissues in the terahertz frequency band," *J. Infr., Millim., THz Waves*, vol. 34, no. 9, pp. 529–538, Sep. 2013.

[18] O. Spathmann, M. Zang, J. Streckert, V. Hansen, M. Saviz, T. M. Fiedler, K. Statnikov, U. R. Pfeiffer, and M. Clemens, "Numerical computation of temperature elevation in human skin due to electromagnetic exposure in the THz frequency range," *IEEE Trans. THz Sci. Technol.*, vol. 5, no. 6, pp. 978–989, Nov. 2015.

[19] K. Jerbic, B. Sievert, J. T. Svejda, A. Rennings, and D. Erni, "On the applicability of homogenization in composite material models for tisse analysis in the mm-wave range," in *Proc. Photon. Electromagn. Res. Symp./Prog. Electromagn. Res. (PIERS)*. Rome, Italy: Univ. Rome La Sapienza, 2019, pp. 1–15.

[20] S. Huclova, "Modeling of cell suspensions and biological tissue for computational electromagnetics," Ph.D. dissertation, ETH Zurich, Zurich, Switzerland, 2011.

[21] H. Richter, "Mote3D: An open-source toolbox for modelling periodic random particulate microstructures," *Model. Simul. Mater. Sci. Eng.*, vol. 25, no. 3, Apr. 2017, Art. no. 035011.

[22] I. Krakovský and V. Myroshnychenko, "Modeling dielectric properties of composites by finite-element method," *J. Appl. Phys.*, vol. 92, no. 11, pp. 6743–6748, Dec. 2002.

[23] COMSOL AB. *COMSOL Multiphysics (V. 5.4)*. Accessed: Mar. 7, 2020. [Online]. Available: http://www.comsol.com

[24] A. H. Sihvola, *Electromagnetic Mixing Formulas and Applications* (IEEE Electromagnetic Waves Series), vol. 47. London, U.K.: Institution of Electrical Engineers, 2008.

[25] G. Solomakha, J. T. Svejda, C. van Leeuwen, A. Rennings, A. J. Raaijmakers, S. Glybovski, and D. Erni, "A self-matched leaky-wave antenna for ultrahigh-field MRI with low SAR," 2020, *arXiv:2001.10410*. [Online]. Available: http://arxiv.org/abs/2001.10410

[26] B. Cabral and L. C. Leedom, "Imaging vector fields using line integral convolution," in *Proc. 20th Ann. Conf. Comput. Graph. Interact. Techn.*, M. C. Whitton, Ed., New York, NY, USA, 1993, pp. 263–270.
[27] S. Eddins. *Network Visualization Based on Occlusion Sensitivity: Mathworks Blogs*. Accessed: Jan. 28, 2019. [Online]. Available: https://blogs.mathworks.com/deep-learning/2017/12/15/network-visualization-based-on-occlusion-sensitivity/
[28] D. A. G. Bruggeman, "Berechnung verschiedener physikalischer konstanten von heterogenen substanzen," *Annalen der Physik*, vol. 416, no. 7, pp. 636–664, 1935.
[29] L. D. Landau, E. M. Lifshits, and L. P. Pitaevskiĭ, *Electrodynamics of Continuous Media* (Course of Theoretical Physics), vol. 8. Oxford, U.K.: Pergamon, 1984.
[30] H. Looyenga, "Dielectric constants of heterogeneous mixtures," *Physica*, vol. 31, no. 3, pp. 401–406, Mar. 1965.
[31] A. H. Sihvola and J. A. Kong, "Effective permittivity of dielectric mixtures," *IEEE Trans. Geosci. Remote Sens.*, vol. 26, no. 4, pp. 420–429, Jul. 1988.
[32] T. Hanai, "Theory of the dielectric dispersion due to the interfacial polarization and its application to emulsions," *J. Appl. Phys.*, vol. 171, no. 1, pp. 23–31, 1960.
[33] K. Asami, "Characterization of heterogeneous systems by dielectric spectroscopy," *Prog. Polym. Sci.*, vol. 27, no. 8, pp. 1617–1659, Oct. 2002.

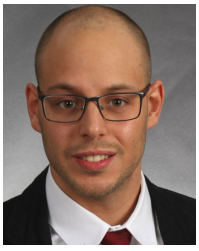

KEVIN JERBIC received the B.Sc. and M.Sc. degrees in electrical engineering from the University of Duisburg-Essen, Duisburg, Germany, in 2015 and 2017, respectively. Since 2017, he has been working as a member of the Department of General and Theoretical Electrical Engineering, University of Duisburg-Essen. His current research interests include the development of model based calibration schemes for the classification of material properties of complex material systems using machine learning approaches based on artificial neural networks at mm-wave frequencies. This includes the exploration of validity limits of hierarchical multiscale approaches for numerical homogenization to capture the dispersive and tensorial macroscopic electromagnetic properties of (bio-)composites and the quantification of the contribution of rough interfaces to subsurface scattering.

KEVIN NEUMANN received the B.Sc. degree in nanoengineering and the M.Sc. degree in power engineering from the University of Duisburg-Essen, in 2015 and 2017, respectively. He is currently pursuing the Ph.D. degree with the Department of General and Theoretical Electrical Engineering (ATE), Duisburg, Germany, working on the DFG project "Flexible Radio Frequency Identification Tags and System (FlexID)". His research interests include the full system development of chipless RFID tags, which involves semiconductor modeling as well as electromagnetic wave simulations. Furthermore, he investigates the performance of numerical crumpled antenna structures using a combination of finite element and boundary element method modeling.

JAN TARO SVEJDA started his electrical engineering career at the University of Applied Science, Düsseldorf, Germany. He received the B.Sc. degree from the University of Applied Science, in 2008, and the M.Sc. and Dr.-Ing. degrees in electrical engineering and information technology from the University of Duisburg-Essen, Duisburg, Germany, in 2013 and 2019, respectively, for his research work in the field of X-nuclei based magnetic resonance imaging. He is currently working as a Research Assistant with the Department of General and Theoretical Electrical Engineering, University of Duisburg-Essen, where he is involved in teaching several lectures and courses mainly in the field of electrical engineering. His research interests include all aspects of theoretical and applied electromagnetics, currently focusing on medical applications, electromagnetic metamaterials, and scientific computing methods.

BENEDIKT SIEVERT (Member, IEEE) was born in Krefeld, Germany. He received the B.Sc. and M.Sc. degrees in electrical engineering/high frequency systems from the University of Duisburg-Essen, in 2017 and 2019, respectively. Since 2017, he has been a member of the Laboratory of General and Theoretical Electrical Engineering, University of Duisburg-Essen. His current research interests include mm-wave on-chip antennas, electromagnetic metamaterials, and theoretical and computational electromagnetics.

ANDREAS RENNINGS studied electrical engineering at the University of Duisburg-Essen, Germany. He carried out his diploma work during a stay at the University of California in Los Angeles. He received the Dipl.-Ing. and Dr.-Ing. degrees from the University of Duisburg-Essen, in 2000 and 2008, respectively. From 2006 to 2008, he was with IMST GmbH, Kamp-Lintfort, Germany, where he worked as an RF Engineer. Since then, he has been a Senior Scientist and a Principal Investigator with the Laboratory for General and Theoretical Electrical Engineering, University of Duisburg-Essen. His research interests include all aspects of theoretical and applied electromagnetics, currently with a focus on medical applications and on-chip millimeter-wave/THz antennas. He received several awards, including a student paper prize from the 2005 IEEE Antennas and Propagation Society International Symposium and the VDE-Promotionspreis 2009 for his dissertation.

DANIEL ERNI (Member, IEEE) received the diploma degree from the University of Applied Sciences Rapperswil (HSR), in 1986, the diploma degree from ETH Zürich, in 1990, all in electrical engineering, and the Ph.D. degree from the Laboratory for Electromagnetic Fields and Microwave Electronics, ETH Zürich, in 1996. Since 1990, he has been working with the Laboratory for Electromagnetic Fields and Microwave Electronics, ETH Zürich. From 1995 to 2006, he was the Founder and the Head of the Communication Photonics Group, ETH Zürich. Since October 2006, he has also been a Full Professor of general and theoretical electrical engineering with the University of Duisburg-Essen, Germany. His current research interests include nanophotonics, plasmonics, optical antennas, as well as advanced solar cell concepts, optical and electromagnetic metamaterials (e.g., for multi-functional leaky wave antennas and for advanced RF systems for high-field MRI imaging), microwave engineering and THz modeling (e.g., for chipless RFID tags and for THz material and surface characterization), computational electromagnetics, and bioelectromagnetics (e.g., biological tissue modeling). On the system level, he has pioneered the introduction of numerical structural optimization into dense integrated optics device design. Further research interests include science and technology studies (STS) as well as the history and philosophy of science with a distinct focus on epistemology in engineering sciences. He is also a Co-Founder of the spin-off company airCode on flexible printed chipless RFID technology. He is also a Fellow of the Electromagnetics Academy, a member of the Center for Nanointegration Duisburg-Essen (CENIDE), as well of Materials Chain, the Flagship Program of the University Alliance Ruhr, and a member of the Swiss Physical Society (SPS), the German Physical Society (DPG), the Optical Society of America (OSA), and Electrosuisse.